

How do depth of discharge, cycle number and calendar age affect capacity retention and electrode stack growth in Li-ion cells?

Roby Gauthier^a, Aidan Luscombe^a, Toby Bond^{a,b}, Michael Bauer^a, Michel Johnson^a, Jessie Harlow^a, Alex Louli^a, J.R., Dahn^{a*}

^aDepartment of Physics and Atmospheric Science, Dalhousie University, Halifax B3H 4R2, Canada

^bCanadian Light Source, Saskatoon S7N 2V3, Canada

**jeff.dahn@dal.ca*

Lithium-ion cells undergoing different depths of discharge, different numbers of cycles and having different ages have different degrees of lithium inventory loss, impedance growth and active mass loss. Here, a large matrix of NMC622/graphite Li-ion pouch cells were tested with seven different state of charge ranges (0-25, 0-50, 0-75, 0-100, 75-100, 50-100 and 25-100%), three different C-rates and at two temperatures. Cells were cycled for 2.5 years before detailed analysis by dV/dQ analysis, lithium-ion differential thermal analysis, volume expansion by Archimedes' principle, electrode stack growth, ultrasonic transmissivity and x-ray computed tomography. These measurements enabled us to develop a complete picture of cell aging for these cells. This then led to an empirical predictive model for cell capacity loss versus SOC range, cycle number and calendar age, where the only contributing factors were lithium inventory loss and impedance growth. Although these particular cells exhibited substantial positive electrode active mass loss, this did not play a role in capacity retention because the cells were anode limited during full discharge under all the tests carried out here. However, the

positive electrode mass loss was strongly coupled to positive electrode swelling and electrolyte “unwetting” that would eventually cause dramatic failure.

Introduction

As the world rapidly turns to electric vehicles as a mode of transportation and to electrical energy storage systems for solar and wind power, predicting and improving the long-term performance of lithium-ion batteries is crucial. Researchers often use full charge and discharge protocols to determine and predict Li-ion cell lifetime.^{1–4} However, since many users rarely drive long distances daily or deplete energy storage systems completely, those protocols do not represent realistic duty cycles well for battery electric vehicles (BEV) or electrical energy storage systems.^{5–7} As a result, analyzing the impact of the depth of discharge (DOD) and state of charge (SOC) range on cell lifetime is important to understand cell degradation in real applications. The effect of DOD and SOC range on lifetime and other cell parameters has been studied before.^{8–22} However, there are few experimental studies on a large SOC range/rate/temperature matrix of cells that also include an extensive study of the changes which have occurred to the cells after years of testing.

One of the primary causes of cell capacity fade, the growth of the negative electrode solid-electrolyte interface (SEI), which leads to lithium inventory loss, is still not well understood. Many different mechanisms have been proposed to explain the continuous growth of the SEI on the graphite electrode after formation: diffusion of the electrolyte through nanosized SEI pores, electron tunneling, electron conduction or interstitials diffusion of neutral lithium through the SEI, “near-shore” SEI aggregation or SEI cracking.^{8,23,24} A detailed study of the effect of depth

of discharge and state of charge range on cell capacity loss can help researchers determine how these factors influence SEI growth.

For this study, a large matrix of cells which consisted of two different cycling temperatures (20°C and 40°C), three different cycling rates (C/10, C/5, C/3), seven different SOC ranges (0-25, 0-50, 0-75, 0-100, 75-100, 50-100 and 25-100%) was created, for a total of 96 cells. The cells consisted of polycrystalline NMC622/natural graphite (NMC622/NG) cells with VC211 (2% vinylene carbonate (VC) + 1% methylene methane disulfonate (MMDS) + 1% tris-trimethylsilyl phosphite (TTSPi)) as an additive blend in 1.2M LiPF₆ EC:EMC 3:7 or 1.2M LiPF₆ EC:DMC 3:7 electrolyte. The VC211 additive blend was chosen because of its good performance in cells.²⁵ Natural graphite was used because of its large expansion during charging, which might create SEI cracking.²⁶ Polycrystalline NMC622 was used to study the effect of SOC range or DOD on the microcracking of the positive electrode. As a result, the cells used in this work are not intended to be as good as the ‘million-mile battery’ of Harlow et al.,²⁷ instead they are intended to help researchers develop a deeper understanding of the degradation of lithium-ion cells.

Experimental Methods

Pouch cells. —Li(Ni_{0.6}Mn_{0.2}Co_{0.2})O₂ (NMC622)/graphite (gr) 402035-size pouch cells were received dry (i.e., with no electrolyte) from Li-Fun Technology (Zhuzhou, Hunan, China). This work utilized two different NMC622 positive electrode active materials: one with an Al₂O₃ coating (NMC622A) and the other with a proprietary coating (NMC622B).^{28,29} The cell capacities at 4.3 V were ~250 mAh during formation for both cell types. After formation, the capacity at 4.1 V and C/10 was ~220 mAh. The NMC622 active material used in this work was

composed of conventional secondary spherical agglomerations of smaller (hundreds of nm) primary particles. Before cells were filled with electrolyte, they were cut open in an argon-atmosphere environment and dried under vacuum at 80°C for 14 hours. Detailed information about the pouch cells can be found in Table S1 and Table S2.

Electrolyte preparation. —In most cases, the control electrolyte used was 1.2M LiPF₆ in a 3:7 mixture by weight of EC (BASF, 99.95%, < 20 ppm water) and EMC (BASF, 99.9%, < 20 ppm water), respectively. However, for the cells that cycled at 20°C, the control electrolyte used was 1.2M LiPF₆ in a 3:7 mixture by weight of EC and DMC (BASF, < 20 ppm water). VC211 ternary blend was used as the additive, which consists of 2 wt% VC (BASF, 99.5%, < 100 ppm water), 1 wt% TTSPi (Tokyo Chemical Industry Co., Ltd. (TCI), > 95.0%) and 1 wt% MMDS (Guangzhou Tinci Co. Ltd, 98.70%).

The cells were filled with electrolyte in an argon-atmosphere environment and then vacuum-sealed at a gauge pressure of −90 kPa and a temperature of 165°C using a compact vacuum sealer (MSK-115A, MTI Corp.). All electrochemical measurements reported in this work were performed on a minimum of two replicate pouch cells, to ensure experimental precision.

Formation. —Following filling with electrolyte, cells were maintained at 1.5 V and at room temperature for 24 h to allow time for the electrolyte to fully wet the electrodes. The cells were then moved into temperature boxes at 40.0 ± 0.1°C and connected to a Maccor series 4000 battery tester for formation. First, cells were held at 1.5 V for 30 min to allow time for the temperature to stabilize and then they were charged at C/20 to 4.3 V. Cells were maintained at 4.3 V for one hour and then discharged at C/20 to 3.8 V. The electrolyte of each cell reduced

during the first charge to form the initial SEI on the graphite at a cell voltage of 2.4 V and the cells produced ~0.3 mL of gas. Cells were degassed after formation and sealed again. After formation, the EIS Nyquist plot of the cells had a semi-circle diameter (R_{CT}) of ~40 $\Omega \cdot \text{cm}^2$ (see Figure S1).

Long term cycling test. —48 cells were placed in a temperature-controlled chamber at 40.0 ± 0.1 °C connected to a Neware battery cycler, while 48 cells were connected to a Neware battery cycler at room temperature (20 ± 2 °C). 24 of the cells at 40°C were NMC622A/NG cells, while the rest were NMC622B/NG cells. The cells at room temperature were NMC622A/NG cells. The voltage ranges used for long-term cycling of each NMC622A/NG cell are summarized in Table 1 and the voltage ranges used for each NMC622B/NG cell are summarized in Table 2. Each voltage range is associated with an approximate depth of discharge (DOD) or SOC range.

Table 1: Voltage ranges applied to the NMC622A/NG cells. 18 cells are cycling for each voltage range. 12 cells at room temperature (20°C) and six cells at 40°C. This corresponds to 72 cells in total. These cells will be called fixed upper cutoff cells (UC cells).

	100% DOD 100-0% SOC	~75% DOD 100-25% SOC	~50% DOD 100-50% SOC	~25% DOD 100-75% SOC
Upper cutoff voltage	4.1 V	4.1 V	4.1 V	4.1 V
Lower cutoff voltage	3.0 V	3.495 V	3.6 V	3.77 V

Table 2: Voltage ranges applied to the NMC622B/NG cells. Six cells are cycling for each voltage range, for a total of 24 cells. All are at 40°C. These cells will be called fixed lower cutoff cells (LC cells).

	100% DOD 100-0% SOC	~75% DOD 75-0% SOC	~50% DOD 50-0% SOC	~25% DOD 25-0% SOC
Upper cutoff voltage	4.1 V	3.777 V	3.649 V	3.527 V
Lower cutoff voltage	3.0 V	3.0 V	3.0 V	3.0 V

For each voltage range, three pairs of UC or LC cells were cycled at three different C-rates:

C/10, C/5, and C/3, except for the cells at 20°C. In the 20°C case, three quartets of UC cells were cycled at these three different C-rates. Quartets were used instead of doublets, since some data (100% SOC range checkup cycles) was missing before ~2000 hours of testing for the first doublets that cycled for a total of 20000 hours. As a result, a second doublet was cycled under the same conditions for ~7000 hours. The data was then combined to determine the resulting capacity loss over the full 20000 hours and to allow fitting. All NMC622A/NG cells that were not cycled using a full voltage range (3.0 V - 4.1 V) at C/10 had checkup cycles every 500 hours approximately, while all the equivalent NMC622B/NG cells had checkup cycles every 900 hours approximately. The checkup cycles consisted of full range cycles (3.0 V - 4.1 V) at C/10. Each cycle consisted of a CCCV charge and a CC discharge. A CCCV charge consists of a constant current (CC) charge from the lower cutoff voltage (LCV) to the upper cutoff voltage (UCV) followed by a constant voltage (CV) hold at the UCV until the current decreased to C/20. A CC discharge consists of a constant current (CC) discharge from UCV to LCV.

Cell thickness measurements. —The thickness of each pouch cell was measured in the center of the jelly roll region three times using a Mitutoyo linear gage. These three values were then averaged.

Cell volume measurements. —The change in volume of each cell was measured using Archimedes' principle. Cells after filling were suspended under an analytical balance (Shimadzu model AUW220D) by a metal wire and submerged in a beaker full of water and weighed. The process was repeated after formation to determine the volume of gas created during formation. The change in the volume of the cell was then calculated using the apparent change in mass due

to the displacement of water, assuming the density of the water is ~1.00 g/mL. The cell weight under water was measured again after degassing and yet again after long term testing to determine the volume change during long term testing.

UHPC measurements and manual dV/dQ analysis. —Ultra-high precision cycling (UHPC) was performed using the UHPC chargers at Dalhousie University after the cells went through approximately 20000 h of long-term cycling.³⁰ The NMC622/graphite cells were cycled between 3.0 V and 4.1 V at C/40 on the UHPC charger at 40°C after an initial discharge from 3.8 V to 3.0 V. The first V(Q) charging curve of each relevant cell was used to perform a manual dV/dQ analysis which allows us to determine the Li inventory loss and the active mass of each electrode. This dV/dQ analysis was done using the software developed by H. M. Dahn et al.³¹

Automatic dV/dQ analysis on long-term cycling data. —Long-term Neware cycling data was automatically analyzed using a program written using the MATLAB R2020a software.³² In the case of cells with checkup cycles, only the checkup cycles were analyzed and the remaining main cycles were discarded by the program. The program operates similarly to the software developed by H. M. Dahn et al., however instead of using a nonlinear least squares fitting algorithm (Levenberg-Marquardt method) to fit the calculated dV/dQ vs. Q curve to the experimental dV/dQ vs. Q curve, the program developed in this work calculated Chi-square from the difference between the theoretical and experimental dV/dQ vs Q curves for **all** negative electrode slippage, positive electrode slippage, negative active mass and positive active mass values within a discrete 4D matrix and selected the electrode mass and slippage values corresponding to the smallest Chi-squared. From now on, this method will be called the dV/dQ

Matrix method. While the dV/dQ Matrix method is more computationally expensive than the Levenberg-Marquardt method, it gave the authors a higher confidence in the results, since the dV/dQ Matrix method can help confirm that the global minimum has been found, if the matrix range is large enough. The automatic dV/dQ analysis was applied to the Neware data of a specific cell using the dV/dQ Matrix method on N equally spaced cycles from 0 hour to ~20000 hours. The 4D matrix used for each cycle was a 150 x 75 x 10 x 5 matrix (positive electrode slippage precision x positive active mass precision x negative electrode slippage precision x negative active mass precision). When N = 6, the computational time for this matrix size was ~10 minutes per cell. The positive electrode slippage was scanned from -0.5 mAh to 75 mAh, the positive active mass was scanned from 0.9 g to 1.64 g, the negative electrode slippage was scanned from 0 mAh to -10 mAh and the negative active mass was scanned from 0.98 g to 1.08 g. The scanning range was guided by the results of manual dV/dQ vs. Q analysis. The program possesses a second mode which allows one to fix the negative electrode mass and negative electrode slippage to reasonable values. This is possible for our cells since these values do not seem to change dramatically when the program uses a 4D matrix instead (see Figure S2). This allows the program to form an image from the matrix, which is now a 2D matrix, since the two additional dimensions are now fixed. To get a more interesting image, the negative value of the base 10 logarithm of the Chi-squared value was plotted instead of the Chi-squared value.

Differential thermal analysis. —Lithium-ion differential thermal analysis (Li-ion DTA) is a non-destructive method of probing the state of the electrolyte inside a Li-ion cell. This method, first developed by Day et al, involves cooling the cell down to a cryogenic setpoint where the electrolyte in the cell is entirely frozen, and tracking the temperature of the cell as it heats back

to room temperature at a constant, controlled rate.³³

In this case, the lower setpoint was -100.0°C, while room temperature was 25°C. This range was chosen to cover the entire freezing regime of the electrolyte. As well, this range is entirely within the liquid phase of the reference cell, which in this case is 1.0 M LiPF₆ in methyl acetate. This is beneficial, as the reference cell will act very similarly to a sample cell that does not go through phase changes in the regime of interest. In all cases, the cells were cooled at a rate of 3.0 °C/min, held at the low temperature for ten minutes to allow for electrolyte temperature equilibration, and heated at 1.0 °C/min. The direct temperature signals of the sample and reference cells can then be compared to determine the temperatures at which the sample cell underwent phase changes. As these phase changes are sensitive to electrolyte composition, we can identify changes to the electrolyte by comparing DTA curves.

Ultrasonic transmission mapping. —Ultrasonic transmission mapping was performed with an ultrasonic battery scanner (UBSC-LD50, Jiangsu Jitri-Hust Intelligent Equipment Technology Co., Ltd).³⁴ A pair of ultrasonic focus transducers (2 MHz frequency, 30 mm focal distance, customized from Shantou Institute of Ultrasonic Instruments Co., Ltd.) were positioned on either side of the cell. Transducers and cells were immersed in low viscosity silicone oil which serves as an ultrasonic coupling agent. The transducers were installed on a 2-dimensional motion system with a precision of 0.2 mm to perform progressive scanning. The ultrasonic signal was emitted by a transducer on one side of the cell and received by the transducer on the other side. The driving source was a 200 V pulse signal with a pulse width of 250 ns, matching the 2 MHz ultrasonic transducer used here. The waveform of the transmitted signal was recorded with a

collecting card. The peak-to-peak values of received transmission waves were converted into color heat maps to make pseudo color images. Cells were equilibrated at 3.8 V and degassed before the ultrasonic measurements were performed at 20°C.

Computed tomography (CT) scans. — CT scans were collected at the Canadian Light Source synchrotron facility on the Biomedical Imaging and Therapy Insertion Device beamline (BMIT-ID).³⁵ This beamline provides a coherent, highly-collimated, monochromatic x-ray beam with parallel geometry, allowing for enhanced contrast through propagation-based phase imaging. The use of monochromatic beam also minimizes the x-ray dose to the cell, as all incident photons contain sufficient energy to contribute to the acquired image. The high incident flux (3×10^{10} photons/cm²·s) also allows for scans to be acquired many times faster than conventional CT, which limits artifacts from electrolyte motion. All scans were collected using a single-crystal LuAG (Lu₃Al₅O₁₂:Ce) scintillator paired with an optical camera. In this setup, the parallel x-ray projection image is optically magnified, as opposed to magnification using a conventional cone beam source. This makes micron-level imaging of larger objects such as pouch cells possible, as very small sample-to-source distances are not required.

Two different setups were used to image at different scales. A lower-resolution, high-dynamic-range setup was used for imaging liquid electrolyte in the full cell, where a CCD camera (PCO 4000) with an effective pixel size of 8.9 μm was used with a monochromatic beam energy of 70 keV. Cells were scanned using 3000 projections (exposure time = 0.6 seconds) collected over a 180-degree range with the sample placed 40 cm from the detector. A higher-resolution setup was used to scan only the corner of the cells (for electrode thickness measurements) at a

beam energy of 50 keV, where a high-magnification (5x) optical system (manufactured by Optique Peter) was used with an sCMOS camera (PCO Edge), providing an effective pixel size of 1.44 μm . 2500 projections were collected (exposure time = 1.0 seconds) with a sample-detector distance of 3 cm. All scans were reconstructed using the UFO-KIT software package using Paganin phase retrieval.³⁶ This technique processes the self-interference fringes present in synchrotron x-ray projections so that the contrast of the absorption image is enhanced using differences among the refractive indices of materials in the cell. After reconstruction, scans were manually aligned so that electrode planes were parallel to the image axes in the flat portions of the cell, with trilinear interpolation used for image resampling. Thickness measurements were taken manually by measuring the distance between surface planes at the high-contrast cathode/separator boundary.

Pressure measurements. —In-situ stack pressure measurements were performed using the apparatus detailed in Louli et al.³⁷ Pouch cells were volumetrically constrained within a rigid aluminum enclosure such that any volume expansion of the electrode stack would exert a force within the enclosure. The force within the enclosure was measured with subminiature load cells (LCKD-OMEGA Engineering) connected to DP25B-S-A (OMEGA Engineering) strain gauge panel meters. The load cells were fastened in the enclosure with the pouch cell, separated by a force distributing plate. The measured force was converted to kPa using the pouch cell area of 6 cm^2 . For in-situ measurements, the pouch cells were connected to a Neware battery testing system and cycled at C/20 between 3.0 V and 4.1 V. The analog 0-10 V output of the strain gauge panel meter was connected to an adjacent Neware channel to enable simultaneous electrochemical and pressure measurements from both the pouch cell and pressure sensor. These

measurements were performed in a $40.0 \pm 0.1^\circ\text{C}$ temperature box. Finally, the initial pressure at a state of charge (SOC) of 0% was subtracted from the data, so that the “zeroed” pressure at a SOC of 0% was 0 kPa.

Theory

Many models have been used by battery researchers to describe experimental capacity versus cycle/time data. Three types of models can be found in the literature: Empirical models,^{18,38–40} Physical models⁴¹ and Machine learning models.^{42,43} One of the most simple and attractive models is the square root of time model.^{44,45} This model describes the capacity $Q(t)$ as a function of time t according to:

$$Q(t) = Q_0(1 - A\sqrt{t}) \quad (1)$$

, where Q_0 and A are values to fit. This model can be derived by assuming that SEI growth, which results in lithium inventory loss, is inversely proportional to SEI thickness. In other words, we assume that SEI growth is diffusion-limited, but in reality things are much more complicated.⁴⁶ While this model considers the growth of the SEI, it does not consider the effect of impedance growth on capacity loss.⁴⁷ To solve this problem, a first-order impedance term can be added to (1), which is different depending on whether charge capacity Q_c or discharge capacity Q_d is being considered. Additionally, a third term $Q_{CV}(t)$ is added to consider the impact of a constant voltage (CV) charge at 4.1 V, which results in an impedance related capacity gain:

$$Q_c(t) = Q_0(1 - A\sqrt{t}) - \left. \frac{dQ}{dV} \right|_U (\Delta V(t) - \Delta V_0) + Q_{CV}(t) \quad (2)$$

$$Q_d(t) = Q_0(1 - A\sqrt{t}) - \left(\frac{dQ}{dv}\Big|_L + \frac{dQ}{dv}\Big|_U\right) (\Delta V(t) - \Delta V_0) + Q_{cv}(t) \quad (3)$$

, where $\frac{dQ}{dv}\Big|_L$ is the derivative of the capacity with respect to voltage at the LCV during discharge,

$\frac{dQ}{dv}\Big|_U$ is the derivative of the capacity with respect to voltage at the UCV during charge, $\Delta V(t)$ is

the difference between the average charge voltage and the average discharge voltage at time t and ΔV_0 is $\Delta V(t)$ at time $t = 0$. The variable ΔV is closely related to the impedance of the cell by Ohm's law. $Q_{cv}(t)$ can be described by an empirical linear term (see Figure S3). Note that an assumption has been made to write (2) and (3) since we only include the first order impedance term. If the impedance growth is large and/or $\frac{d^2Q}{dv^2}\Big|_L$ or $\frac{d^2Q}{dv^2}\Big|_U$ are large, the second and possibly higher order terms should be included. For example, this is the case if the cell undergoes a rollover failure.⁴⁷ Here, we don't include them since they are negligible in the current work, but one can find a more detailed model and further explanations in the text surrounding Figure S4.

Figures 1a and 1b show the effect of impedance growth on discharge $Q(V)$ curves for two different LCV: 3.0 V and 3.77 V. In this example, exaggerated for clarity, we show three discharge $Q(V)$ curves in both Figures 1a and 1b: The upper $Q(V)$ curves are without impedance effects, the second have a 0.1 V ΔV growth, and the lowest curves have a 0.2 V ΔV growth. Due to the difference in slope of the $V(Q)$ curve at 3.0 V versus at 3.77 V, we see that if a cell is discharged to 3.77 V without a constant voltage step, a much higher impedance related capacity loss can be seen than if the cell is discharged all the way down to 3.0 V. As a first order

approximation, the resulting capacity loss is $\frac{dQ}{dV} \Big|_L (\Delta V(t) - \Delta V_0)$. A similar reasoning can be applied to the constant current part of the charging $Q(V)$ curve, which results in a capacity loss of $\frac{dQ}{dV} \Big|_U (\Delta V(t) - \Delta V_0)$. The $Q_{CV}(t)$ term is necessary to add in the case of CCCV charging but is unnecessary in the case of CC charging. Again, higher order impedance terms should be included in some circumstances.

Figure 1c shows $\frac{dQ}{dV}$ as a function of voltage during charge and discharge of the first cycle of a NMC622A/NG cell. A voltage shift between the charge and discharge $\frac{dQ}{dV}$ can be seen and this is caused by cell impedance. We can also see that a LCV of 3.0 V would result in a much lower impedance related capacity loss than a LCV of 3.4 V (around 18 times less). Note that impedance related capacity loss is reversible and can be recovered by switching to a lower cycling current I , switching to voltage cutoffs with small dQ/dV values or lowering the cutoff current I_s during the end of CCCV charging.

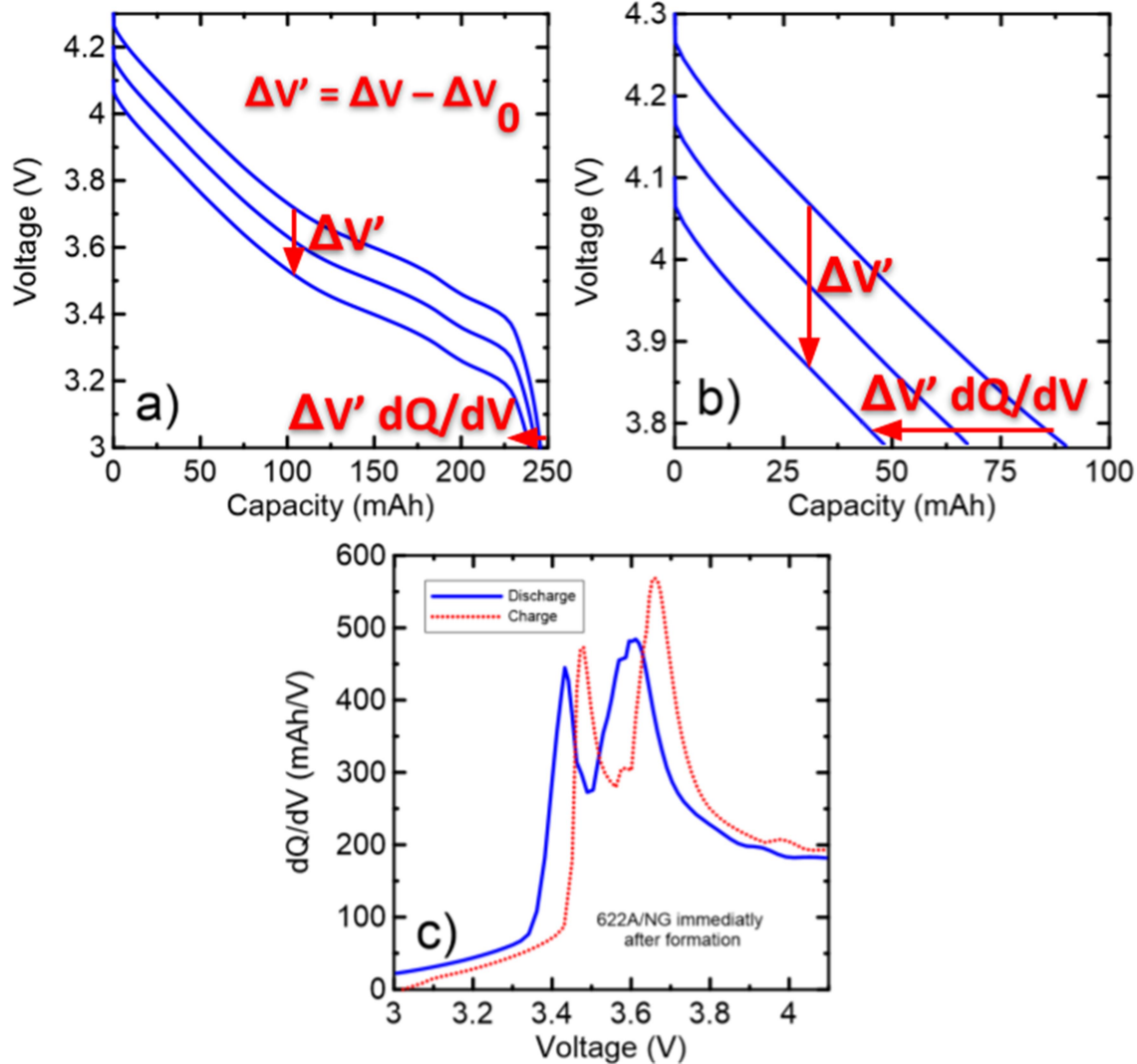


Figure 1: Figures 1a and 1b shows the effect of impedance growth on discharge $Q(V)$ curves for two different LCV: 3.0 V and 3.77 V. The slope of the $Q(V)$ curve at the LCV has an impact on capacity loss. Figure 1c shows the derivative of the capacity with respect to voltage during charge and discharge of NMC622A/NG cells during the first cycle after formation measured at C/20 and at 40°C. The shift between the two curves is mostly due to the non-zero value of ΔV at $t = 0$ which results in a ~ 0.1 V voltage shift.

No term related to cathode mass loss has been included in equations (2) and (3), since capacity

loss mechanisms depend on whether the cell is anode limited or cathode limited. In the case where the cell is anode limited, the capacity loss due to SEI growth is larger than the capacity loss due to cathode mass loss and equations (2) and (3) are correct. However, in the case where the cell is cathode limited, the opposite is true and equations (2) and (3) need to be replaced with:

$$Q_c(t) = Q_0 \left(1 - \frac{m_p(t)}{m_{p0}} \right) - \left. \frac{dQ}{dV} \right|_U (\Delta V(t) - \Delta V_0) + Q_{cv}(t) \quad (4)$$

$$Q_d(t) = Q_0 \left(1 - \frac{m_p(t)}{m_{p0}} \right) - \left(\left. \frac{dQ}{dV} \right|_L + \left. \frac{dQ}{dV} \right|_U \right) (\Delta V(t) - \Delta V_0) + Q_{cv}(t) \quad (5)$$

, where $m_p(t)$ is the positive active mass as a function of time t and m_{p0} is the initial value of m_p .

Note that the cells in this paper are all anode limited, as confirmed by dV/dQ analysis.

Figure 2 shows how we can calculate the lithium inventory loss due to SEI growth, Q_{SEI} , from the half-cell $V(Q)$ curves, which are themselves calculated using dV/dQ vs. Q analysis. We can see the full-cell, anode, and cathode half-cell $V(Q)$ curves before and after cycling, where the capacity of the full cell at top of charge has been fixed at the value from the formation cycle. With this convention, there is no positive electrode slippage as each cell cycle is normalized to the same capacity at the top of charge. From the Figure 2, one concludes that:

$$Q_{SEI} = (\Delta - \Delta_0) + Q_p = (\delta_n - \delta_{n0}) \quad (6)$$

, where $Q_p = Q_0 (1 - m_p/m_{p0})$ is the capacity associated with positive active mass loss in mAh, δ_n

is the absolute negative electrode slippage and δ_{n0} is δ_n before cycling/after formation., $\Delta = \delta_n - Q_p$, $\Delta_0 = \delta_{n0}$. If the cell is anode limited, $\Delta > 0$ and if the cell is cathode limited, $\Delta < 0$.

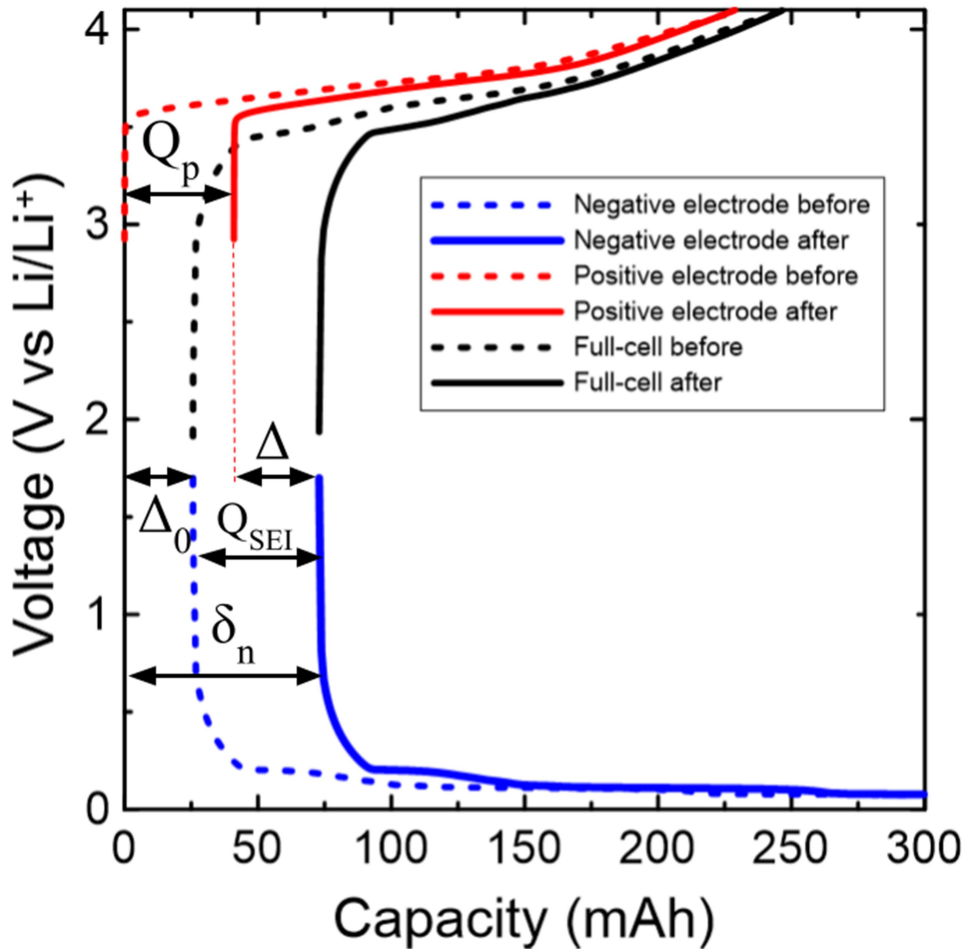


Figure 2: Positive and negative electrode half-cell $V(Q)$ curves and full-cell $V(Q)$ curves before cycling/after formation and after cycling.

There is one additional and final term that may need to be added to equations (2) and (3). At the beginning of testing the cells can be at 3.8 V after EIS measurements for several days. This, then, allows for Li to diffuse into the anode overhang and lithiate it. This lithium content in the overhang may be different than the average lithium content of the negative electrode based on

the SOC range selected for cycling so there may be a small capacity gain or capacity loss during the early cycles of the cell. A term that characterizes diffusion from the overhang/overlap part of the cell needs to be added to our expressions.⁴⁸ In this case, equation (3) becomes (and similarly for equation (2)):

$$Q_d(t) = Q_0(1 - A\sqrt{t}) - \left(\frac{dQ}{dV}\Big|_L + \frac{dQ}{dV}\Big|_U\right) (\Delta V(t) - \Delta V_0) + Q_{CV}(t) \pm Q_{OHL}(1 - e^{-t/\tau}) \quad (7)$$

, where Q_{OHL} is the amount of lithium, in mAh, that diffuses from/to the overhang/overlap and τ is the characteristic time of diffusion, which is on the order of 200-1000 hours.⁴⁸ This last term is more dominant at low cycling temperature (e.g. 20°C) due to the slower diffusion of lithium atoms. Note that the sign and value of Q_{OHL} depend on the average voltage of the cell, the area of the electrodes and the SOC of the overhang/overlap.

Since active particle and SEI cracking are thought to lower the lifetime of a cell, it is also important to have a good understanding of active material expansion during lithiation and to look at the change in pressure of a cycling constrained full cell. Figure 3 shows that during charging of a full cell to 4.1 V, the graphite crystalline structure expands by 6%, while the NMC622 crystalline structure contracts by 2%.^{37,49} While the c-axis of NMC622 expands during charging of the cell to 4.1 V, the a-axis contracts which is the reason for the overall contraction.⁴⁹ However, the overall volume change of the cells during extended cycling not only depends on the crystalline structure of the active materials, but also on the possible cracking of primary and secondary particles, jelly roll deformation and SEI growth.^{26,50,51} These additional contributions might explain the slight slope in the 2 to 2L transition region of graphite in Figure 3b, which is

not present in Figure 3a. Note that gas will be forced to the gas bag and will not be registered in these pressure measurements.

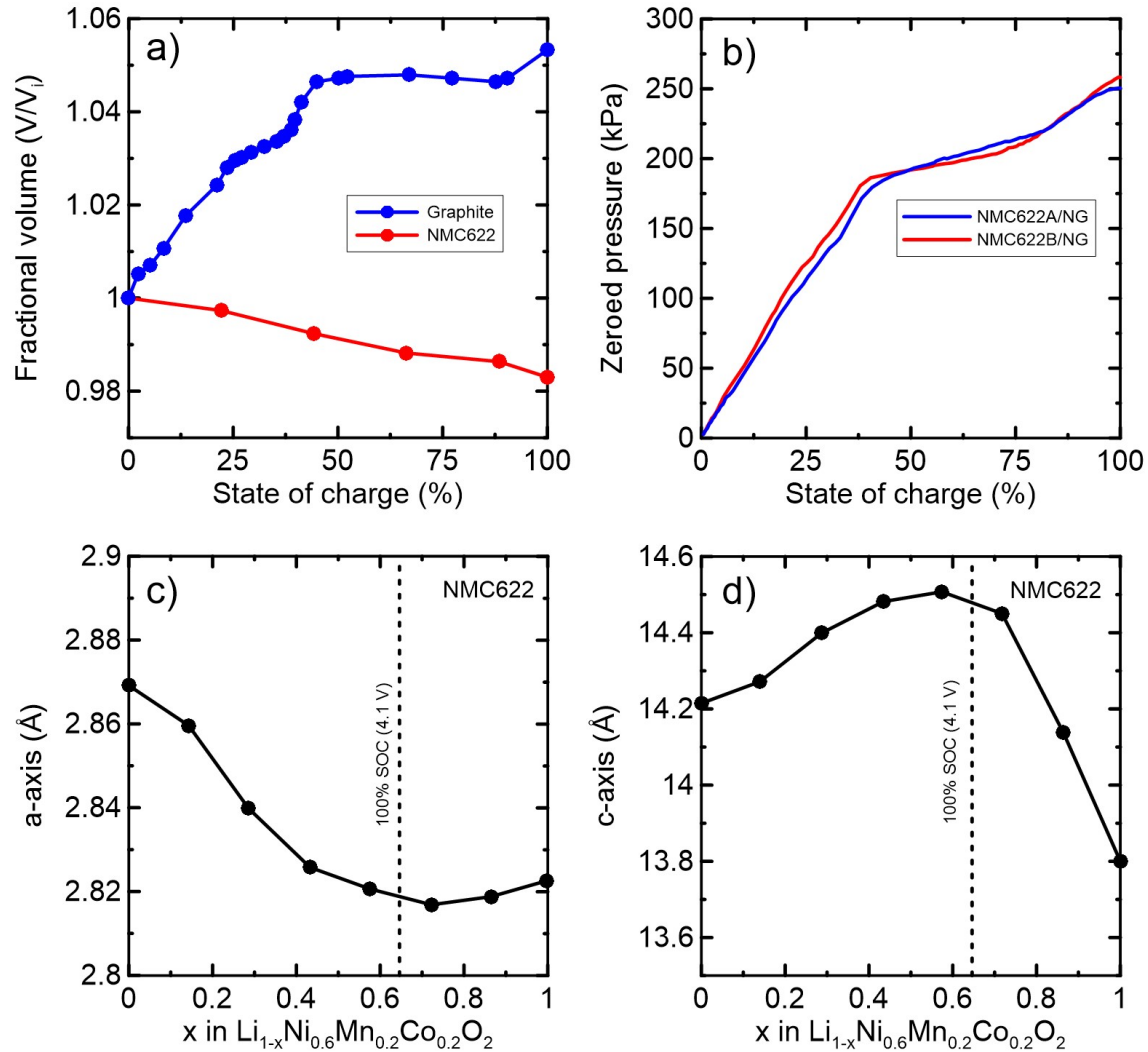


Figure 3: a) Fractional volume change of the unit cell of graphite and NMC622 as a function of state of charge, b) zeroed pressure as a function of state of charge of NMC622A/NG and NMC622B/NG cells, c) a-axis length and d) c-axis length of the unit cell of NMC622 as a function of delithiation. The full state of charge at 4.1 V is indicated for c) and d). For a) and b), a state of charge of 100% is the state of charge that occurs when the cell is at 4.1V. NMC622 data in a), c) and d) were digitized from Lee et al.⁴⁹ and graphite data in a) were digitized from Louli et al.³⁷

Results and Discussion

This research was inspired by the theoretical work of Deshpande and Bernardi, who proposed that capacity loss during cycling should be proportional to the state of lithiation swing squared. They proposed this result by assuming that lithium inventory loss is a consequence of SEI cracking due to expansion and contraction of graphite particles during charge and discharge.⁸ In order to show if this model is indeed correct, a large matrix of cells with different depth of discharge, C-rate and temperature was built as described above.

The current project intended to study cell capacity loss and impedance growth both during and after cycling. Furthermore, the thickness measurements of our cells, differential thermal analysis (DTA) of the electrolyte, ultrasonic transmission mapping and CT scans of our cells gave us insight about the reasons for capacity loss and impedance growth.

After our cells went through their formation protocol, cells were degassed and then connected to a Neware charger and tested at room temperature or in temperature boxes at 40°C. After the cells went through a couple of cycles, the exact DOD value of each cell was calculated and was found to be slightly different than the approximate values predicted in Tables 1 and 2. Figure 4 shows these exact values. For a specific DOD (e.g. ~75% DOD) one can see that the DOD values as a function of C-rate do not change more than $\pm 5\%$. Each plateau in Figure 4 shows the data points of cells at C/10 (red squares), at C/5 (blue circles) and at C/3 (green triangles), respectively from left to right. The LC cells have a smaller DOD than the UC cells by approximately 5%, except for the 100% DOD cells. Furthermore, all cells that permanently cycled in the 3.0 V – 4.1 V

range had their DOD values set to 100% DOD for all C-rates and all cells used the 100% DOD cells at the same C-rate as a reference to calculate their DOD values. The exact DOD values from Figure 4 are used in this work when needed.

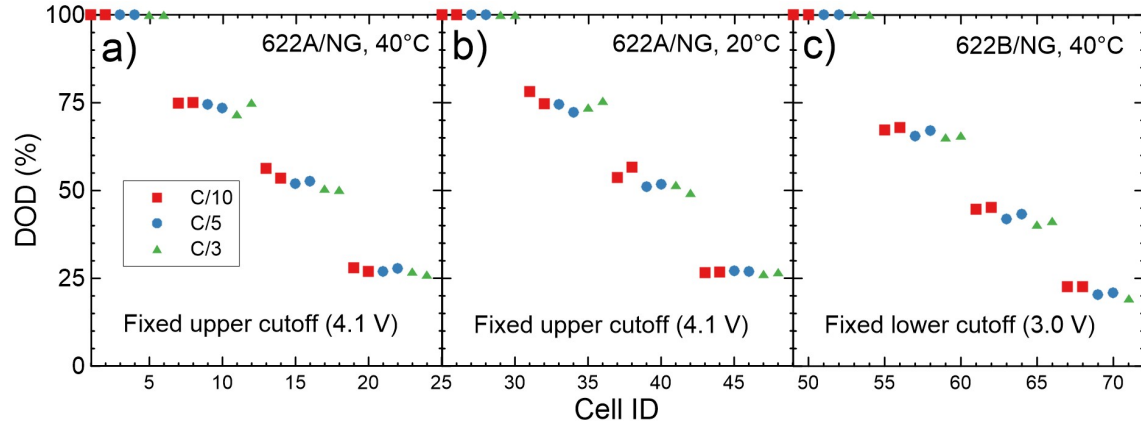


Figure 4: Exact initial DOD values for UC and LC cells at $t \approx 0$ hour. A cell ID is used to identify each cell. For each plateau, the first two data points correspond to cells cycling at C/10 (red squares), the two in the middle to cells cycling at C/5 (blue circles) and the last two to cells cycling at C/3 (green triangles). Each DOD value is calculated using the full-range (3.0 V - 4.1 V) cells at the same rate as a 100% DOD reference. Figure 4a shows the initial DOD values for NMC622A/NG UC cells that cycled at 40°C, Figure 4b for NMC622A/NG UC cells that cycled at 20°C and Figure 4c for NMC622B/NG LC cells that cycled at 40°C.

Each cell was cycled for approximatively 20000 hours using the appropriate protocols, which are mentioned in the Experimental Methods section. Figures 5 to 7 show the discharge capacity and ΔV versus time for all these cells. The b), e), h) columns of these figures show an expanded view of the checkup cycles of these cells, which correspond to the 170-220 mAh region of the data shown in the a), d), g) columns. Each row of these three figures shows the data for a specific C-

rate. Figure 8 shows the capacity loss that was calculated from the checkup cycles for each cell. For cells that missed some initial checkup cycles from 0 to 2000 hours, a linear or square root extrapolation to 0 hour was used to calculate the capacity loss.

Figure 5, 6 and 8 show that at 40°C capacity loss increases when DOD and C-rate increase and that the slope of ΔV vs. time also increases with DOD and C-rate. Also note how cells that cycled at 25% DOD and C/3 have a capacity that is relatively constant around 50 mAh even after 20000 h. Figures 8a and 8b show that capacity losses are similar between UC and LC cells cycling at 40°C, while Figure 8c shows that capacity loss for cells cycling at 20°C is non-linear as a function of DOD because of contributions from overhang/overlap diffusion (see Figure S5). Note that the capacity loss in Figures 8a and 8b is mostly linear versus DOD.

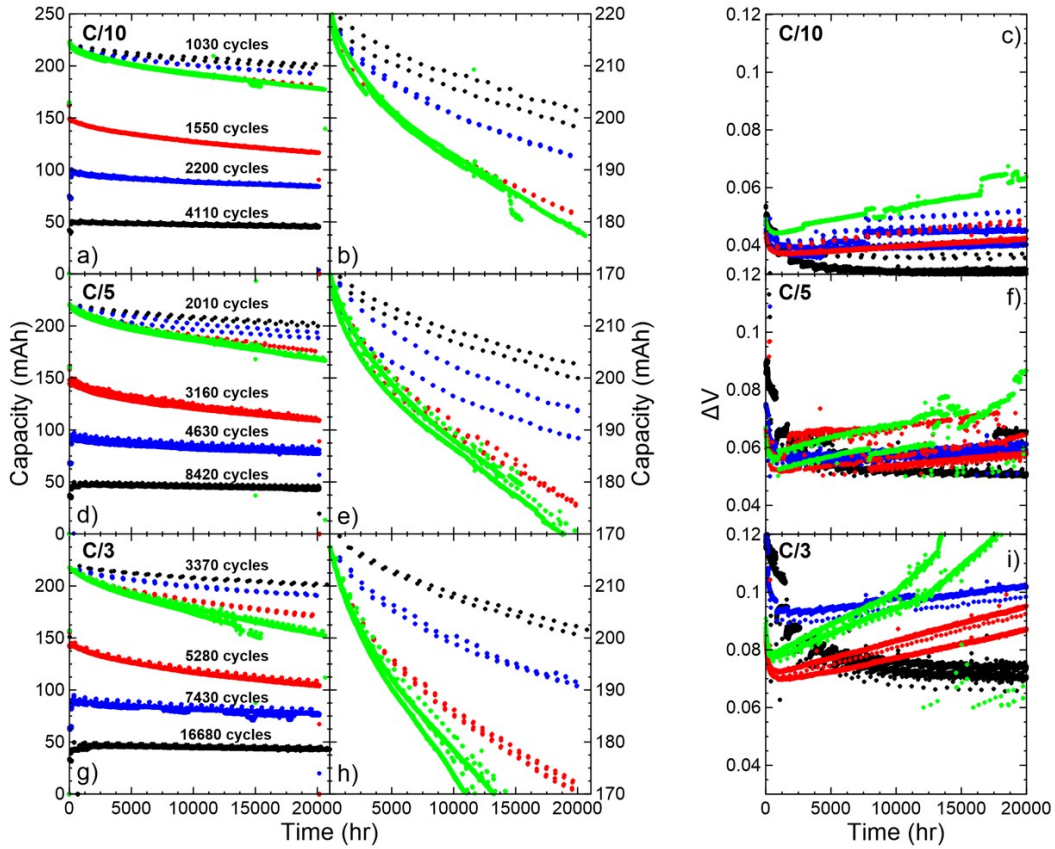


Figure 5: Subfigures a), b), d), e), g), h) discharge capacity versus time and subfigures c), f), i)

ΔV versus time of LC cells that cycled at 40°C. The middle column shows an expanded view of the checkup cycles of the data in the left column. The number of total cycles is also indicated as well as the C-rate. To make the graphs cleaner, the data below 0.045 V in f) and below 0.06 V in i) where removed. This data corresponds to the ΔV values of the checkup cycles and can be found in Figure S6.

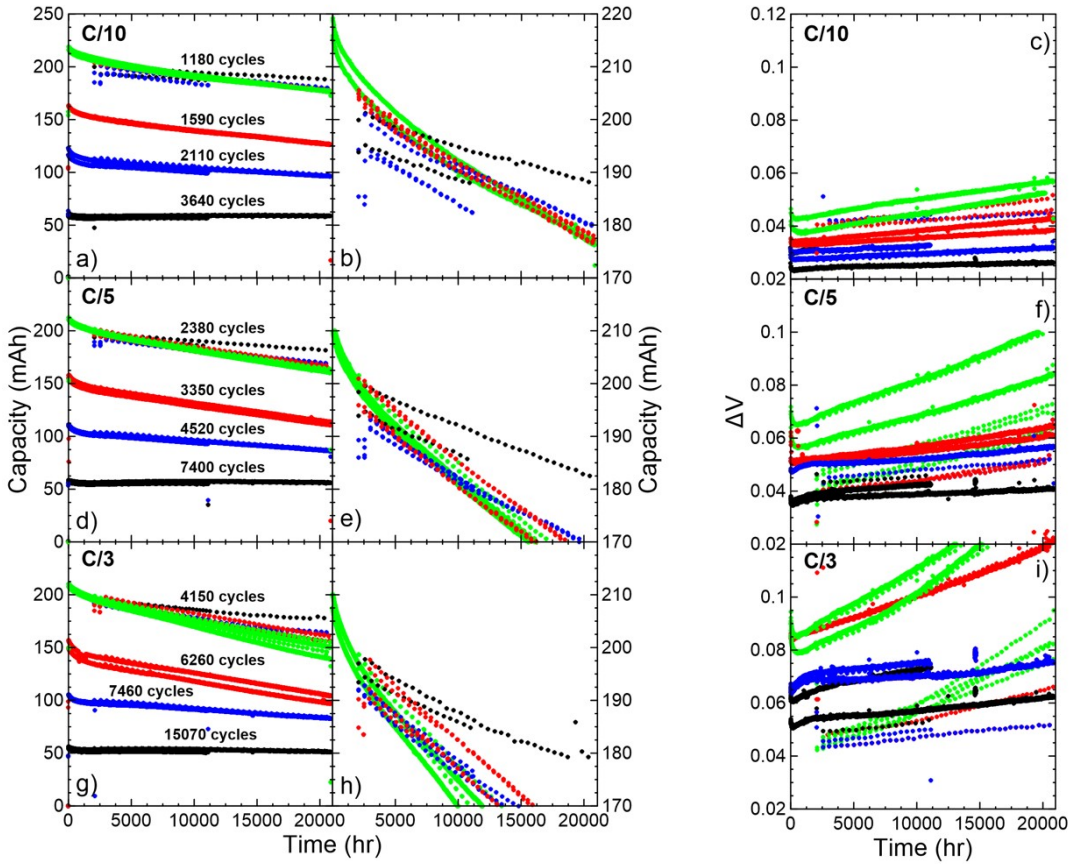


Figure 6: Subfigures a), b), d), e), g), h) discharge capacity versus time and subfigures c), f), i) ΔV versus time of UC cells that cycled at 40°C. The middle column shows an expanded view of the checkup cycles of the data in the left column. The number of total cycles is also indicated as well as the C-rate.

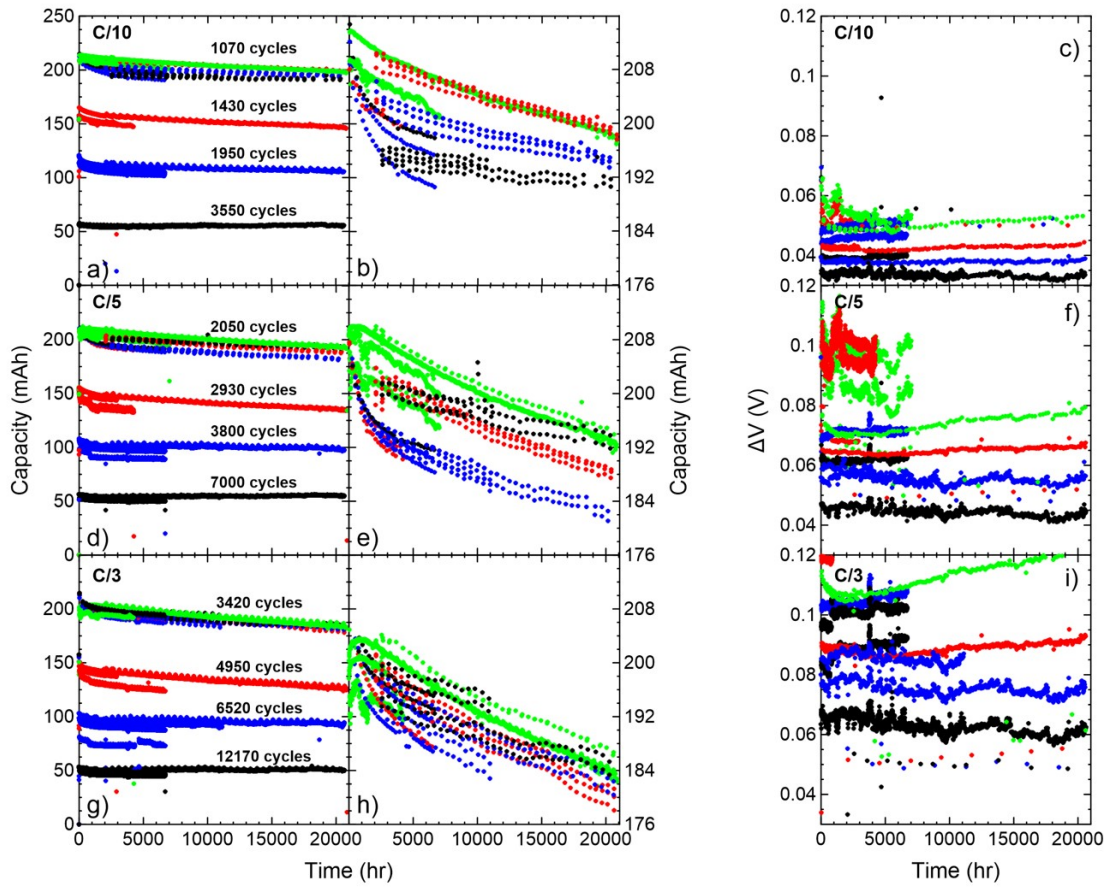


Figure 7: Subfigures a), b), d), e), g), h) discharge capacity versus time and subfigures c), f), i) ΔV versus time of UC cells that cycled at 20°C. The middle column shows an expanded view of the checkup cycles of the data in the left column. The number of total cycles is also indicated as well as the C-rate.

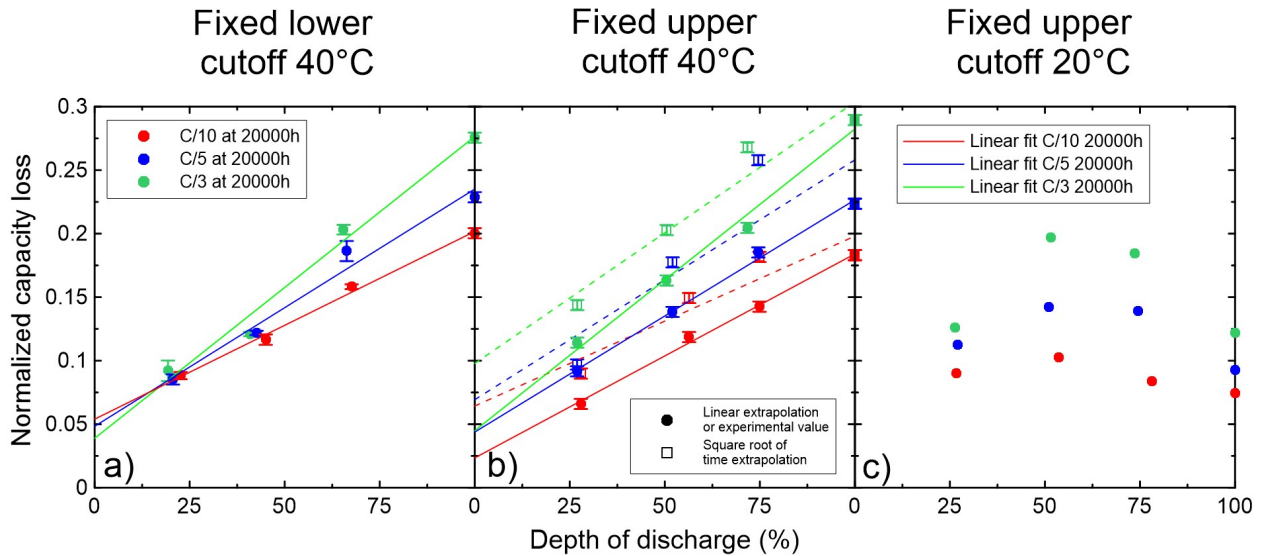


Figure 8: Normalized capacity loss during long-term cycling between 0h and 20000h of a) LC cells that cycled at 40°C, b) UC cells that cycled at 40°C and of c) UC cells that cycled at 20°C. Checkup cycles are used here to calculate capacity loss. Since UC cells are missing their initial checkup cycles, linear extrapolation (solid circles data and solid lines), or square root model extrapolation (open squares data points and dashed lines) to 0 h was used to estimate the capacity loss of the UC cells that cycled at 40°C and a combination with new data was done for the UC cells that cycled at 20°C (see Figure S5 for an example for C/10). Since no data were missing for LC cells, no extrapolation was needed for the data in a). Red, blue, and green data are used to show the results from different C-rate (C/10, C/5, and C/3 in order).

Figure 9 shows the cycles and equivalent full cycles to 90% of the initial capacity for different SOC ranges and C-rates. The results in Figure 9a were obtained by fitting the capacity vs cycle number curves of the cells to a $Q_0(1 - \alpha\sqrt{n})$ behaviour, where Q_0 and α are fitting constants and n is the cycle number. Figures S7 to S12 show these fits, as well as the capacity versus cycle

number data for 100% DOD cells. The results in Figure 9b were obtained by the discrete integration of the capacity versus cycle number curve (including the checkup and main cycles) and by dividing the result by the initial 100% DOD capacity (~ 220 mAh). For example, the 25% DOD LC cells cycling at C/10 achieved 3906 cycles to 90% initial capacity, which corresponds to 874 equivalent full cycles, while the 100% DOD LC cells cycling at C/10 achieved 270 cycles. These values were very similar for UC cells at C/10. However, 25% DOD C/3 LC cells achieved 13372 cycles to 90%, which corresponds to 2611 equivalent full cycles while 25% DOD C/3 UC cells achieved 5917 cycles to 90%, which corresponds to 1542 equivalent full cycles. As expected, the cells that cycle at a low DOD value perform better. Figure S13 shows that the difference between UC cells and LC cells in Figure 9 can be explained by impedance effects. Similar work as in Figure 9 has been done in the past.⁵²⁻⁵⁵

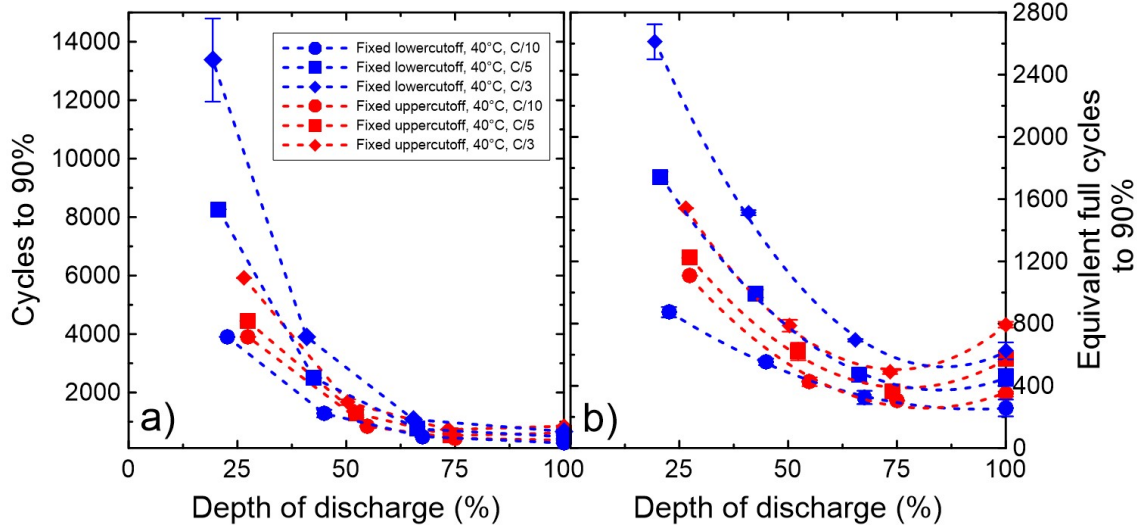


Figure 9: a) Number of cycles before the capacity reaches 90% of the initial capacity and b) number of equivalent full cycles before the capacity reaches 90% of the initial capacity. Blue data correspond to LC cells that cycled at 40°C, while red data correspond to UC cells that cycled at 40°C. Circles, squares or diamonds are used to show the results from different C-rates (C/10, C/5, and C/3, respectively).

Figure 10 show the results of fitting ΔV vs. cycling time from the checkup cycles, for the UC and LC cells that cycled at 40°C, with a linear model of the form $\Delta V(t) = Ct + D$ (see Figures S6 and S14). The parameter C is plotted versus DOD and different colors are used to distinguish data for different C-rates. The results for parameter D, which are the same for all cells, are shown in the right top corner of Figures 10a and 10b. A quadratic fit matches the variation of C versus DOD quite well. Furthermore, while experimental noise is present, the value of C also seems to follow a trend versus C-rate. Since power fade depends on ΔV , understanding these trends is important to better predict the long-term performance of lithium-ion batteries. The data in Figure 10 can be found in Tables S7 to S9, so that it can be compared easily to other data, like pouch cell thickness shown later. The main cycle $\Delta V(t)$ values have also been fitted and the results can be seen in Figures S15 to S18.

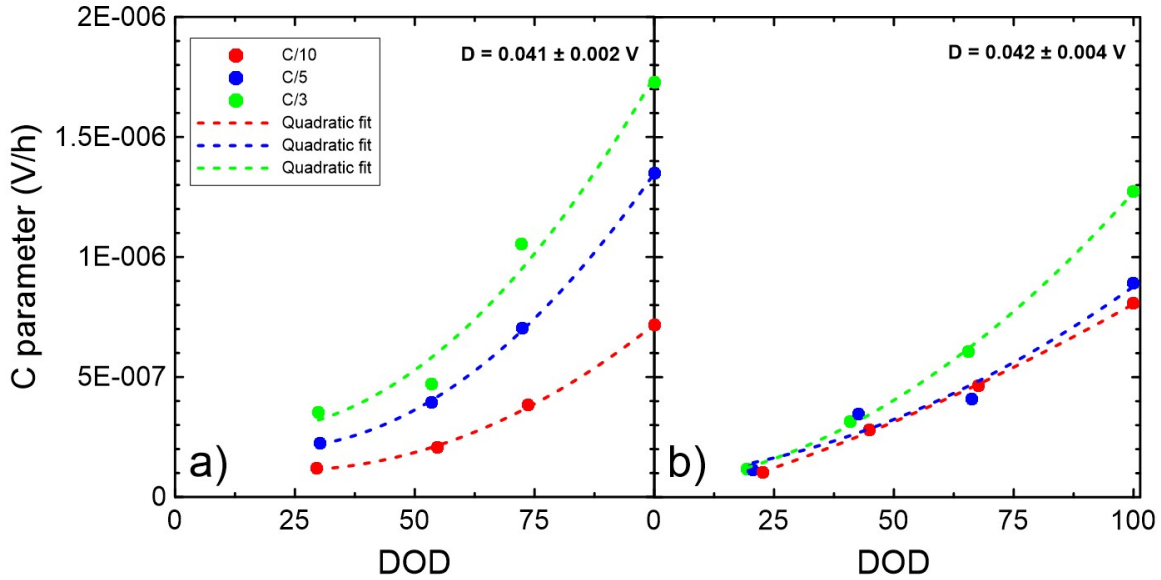


Figure 10: Linear fit results for C using the formula $\Delta V(t) = Ct + D$ for the a) UC cells (Subfigures 6c), 6f), 6i)) and b) LC cells (Subfigures 5c), 5f) and 5i)) at 40°C. The fits were applied to the ΔV values for the checkup cycles only.

Figures 11 and 12 show example results for automatic dV/dQ vs. Q analysis of two UC cells (25% and 100% DOD C/10 UC cells) at various cycle numbers. Figures 11 and 12 show a “heat map” of $-\log \chi^2$ for different possible positive electrode active mass m_p and relative slippage $\Delta = \delta_n - Q_p$, (See Figure 2). Δ is the difference in capacity between the fully lithiated positive and the fully delithiated negative electrodes (See Figure 2) and is used in the calculation of Li inventory loss, Q_{SEI} . (see Equation 6) The χ^2 values represent the least-squares error between the experimental dV/dQ vs Q graph of a cell at a specific cycle number and a dV/dQ calculation using specific m_p and Δ values. The map therefore corresponds to a 2D dV/dQ vs Q scan where the negative electrode mass m_n and the negative electrode slippage³¹ were fixed to values predetermined from a single 4D dV/dQ scan. In these specific cases, the negative electrode mass

m_n was fixed to 1.025 g and the negative electrode slippage was fixed to -1 mAh. In Figures 11 and 12, the center of the dark red ellipse (i.e. $-\log(\chi^2) = 5$) corresponds to the most likely values of Δ and m_p for that cell at that specific cycle number or time, while the blue region (i.e. $-\log(\chi^2) < 2$) corresponds to less likely values for that cell at that specific cycle number or time. Figure 11 shows that the 100% DOD C/10 UC cell lost ~ 0.2 g of its positive active mass after ~ 22000 h of cycling, which corresponds to approximately 15% of the total initial positive active mass, while Δ increased by approximately 10 mAh. Figure 12 shows that the 25% DOD C/10 UC cell lost ~ 0.05 g of its positive active mass after ~ 16000 h of cycling, while Δ increased by approximately 10 mAh.

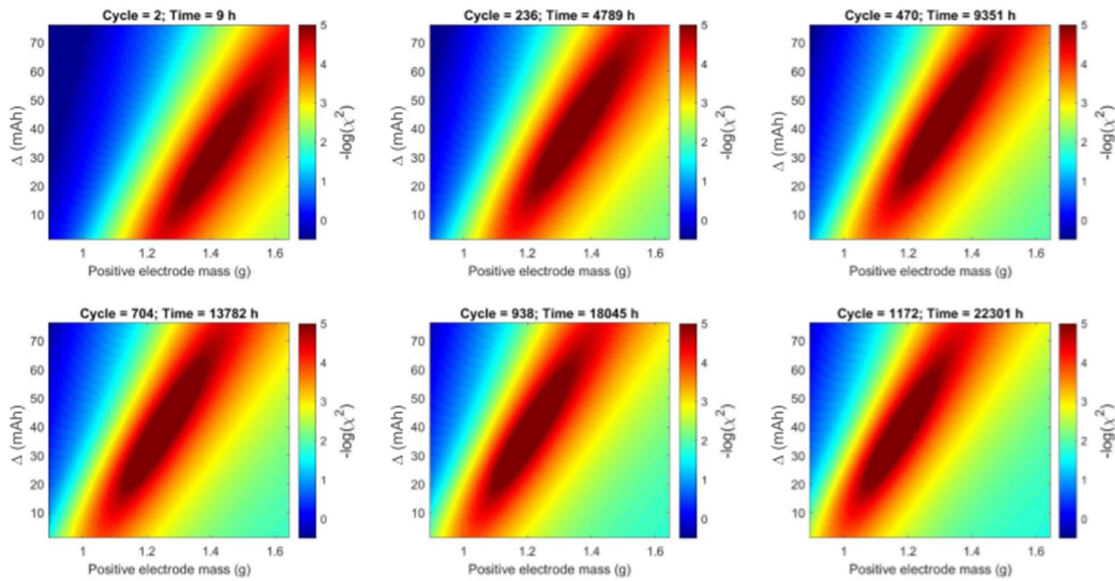


Figure 11: 2D dV/dQ vs Q heat maps of a 100% DOD C/10 UC cell cycled at 40°C for six different times. Multiple $-\log \chi^2$ heat maps are shown as a function of positive electrode active mass m_p and Δ . The negative electrode active mass is kept constant as a function of time.

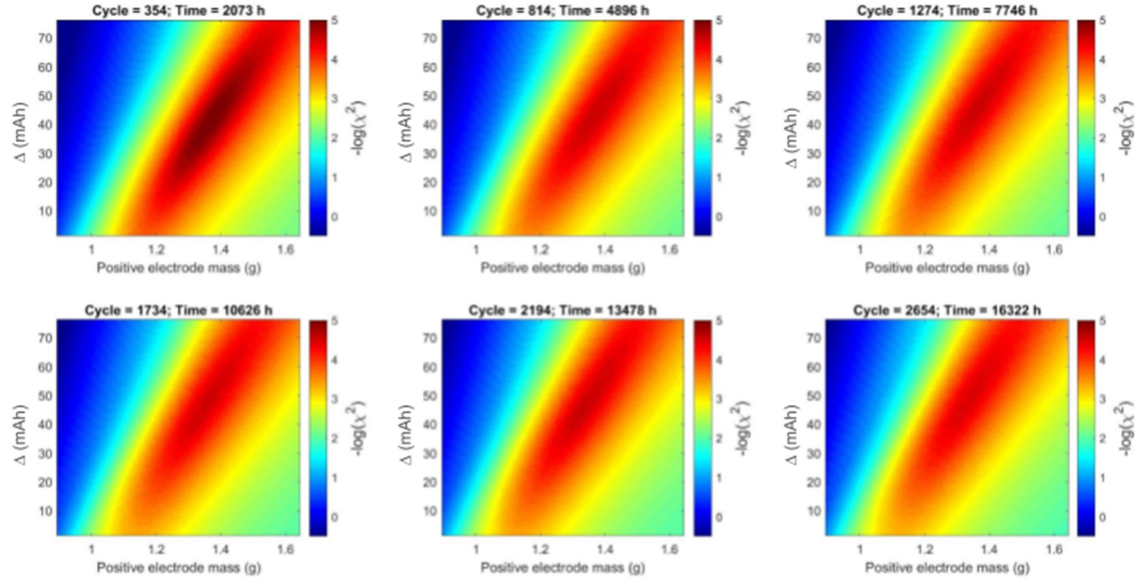


Figure 12: 2D dV/dQ vs Q heat maps of a 25% DOD C/10 UC cell cycled at 40°C for six different times. Multiple $-\log \chi^2$ heat maps are shown as a function of positive electrode mass m_p and Δ . The negative electrode active mass is kept constant as a function of time.

Figure 13 shows the result of a 4D dV/dQ vs Q scan, using the automatic dV/dQ analysis program, of UC and LC cells that cycled for ~ 20000 h at 40°C. The positive electrode active mass and the lithium inventory loss Q_{SEI} are plotted as a function of time. Figure 13 shows that UC cells have a bigger positive electrode active mass loss Δm_p than LC cells at low DOD. This suggest that positive active mass loss occurs more predominantly at high voltage. At high DOD, UC and LC cells have more similar positive active mass losses. Figure 13 shows that the lithium inventory losses are very similar between UC and LC cells for all SOC ranges. This suggest that Q_{SEI} is independent of the average voltage of the SOC ranges, at least for the voltage ranges of the current study. One can find the results for the negative active mass m_n and slippage Δ as a function of time in Figure S2 as well as some of the dV/dQ fits in Figures S19 to S24.

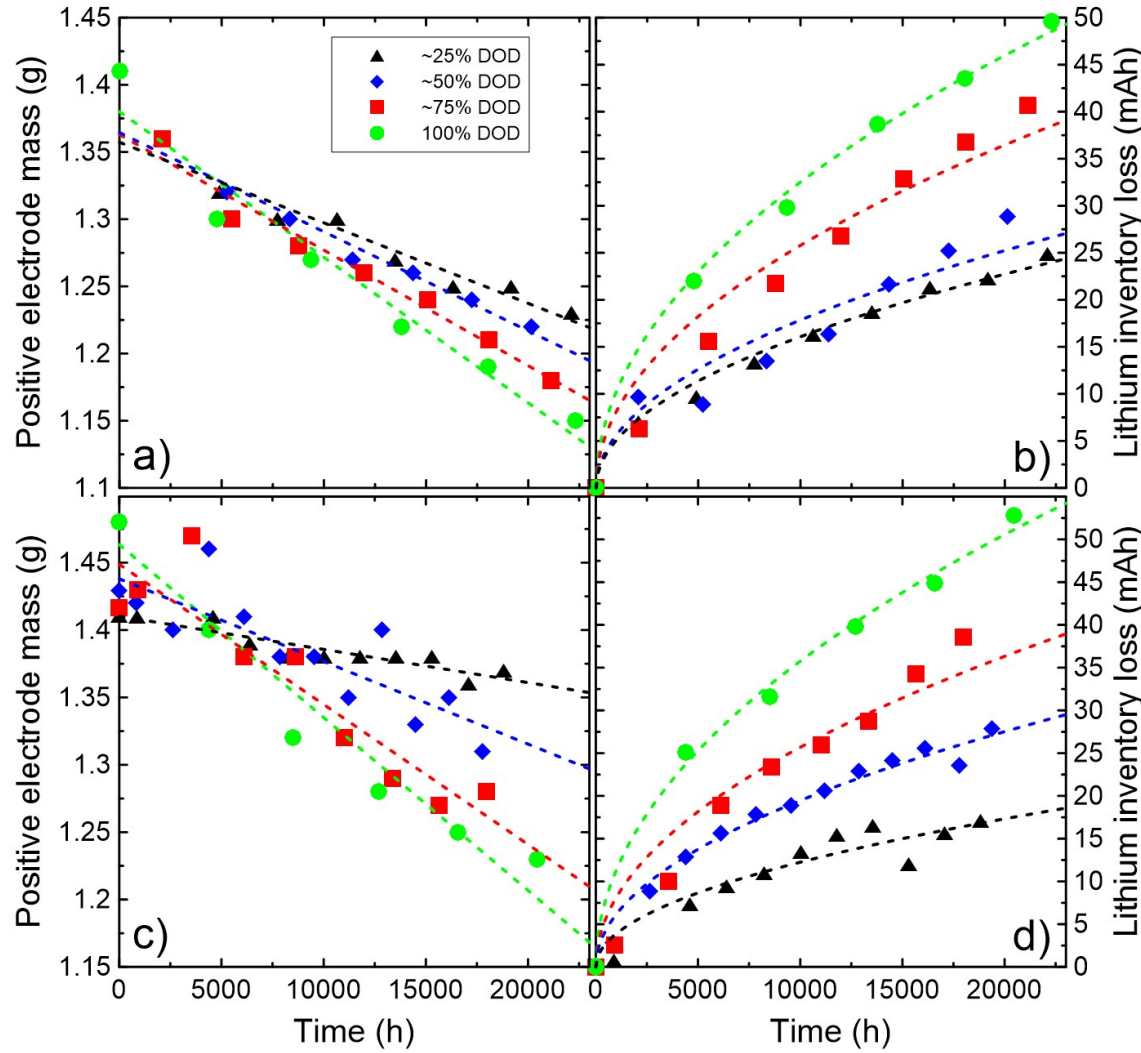


Figure 13: Automatic dV/dQ vs Q scan results for C/10 subfigures a), b) UC and subfigures c), d) LC cells at 40°C as a function of cycling time. Subfigures a) and c) show positive electrode active mass results and subfigures b) and d) show lithium inventory loss results. An automatic 4D dV/dQ vs Q scan was used to get these results. Linear fits (dashed lines in panels a) and c)) and square root time fits (dashed lines in panels b) and d)) were applied to the positive electrode active mass and lithium inventory loss data, respectively, to show likely trends.

Figure 14 shows the positive and negative electrode V(Q) curves vs Li metal obtained from manual dV/dQ analysis on a UHPC charger data before and after long-term cycling at 40°C and

C/10 for 75-100% SOC range, 50-100% SOC range, 25-100% SOC range and 0-100% SOC ranges of UC cells. Figure 14 shows that Q_{SEI} increases as a function of DOD, but the cells are always anode limited even as Δm_p increases with DOD. We also see an increase in positive active mass loss as the DOD value increases.

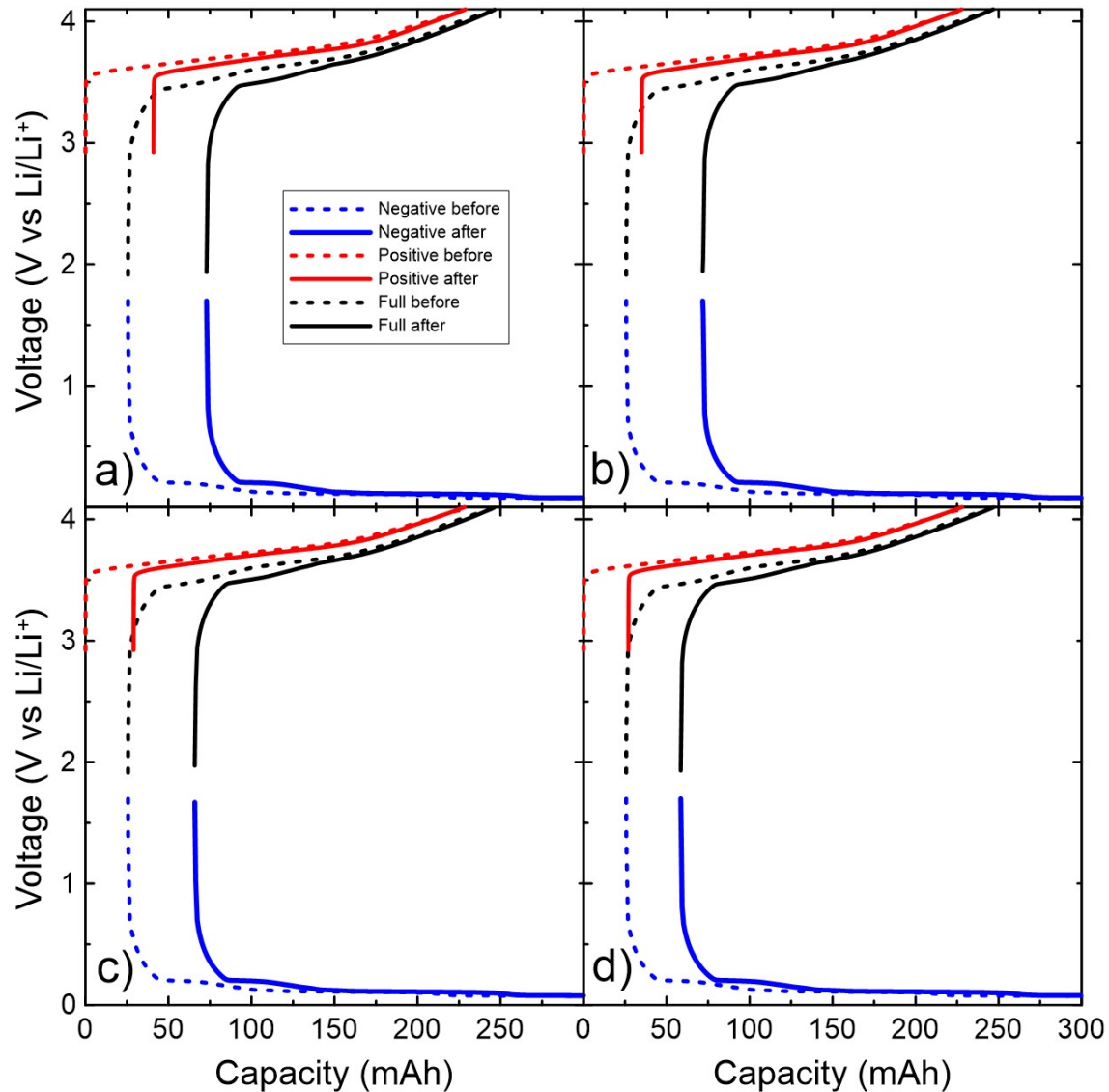


Figure 14: Negative and positive electrode V(Q) curves vs Li/Li⁺ before and after long-term cycling (~20000h) at C/10 and 40°C of a) 0-100% SOC range, b) 25-100% SOC range, c) 50-100% SOC range and 75-100% SOC range for UC cells.

Figure 15 shows that Δm_p increases with SOC range and C-rate for both UC and LC cells at 40°C but the positive active mass loss is much smaller at 20°C for all SOC ranges and C-rates. Again, the positive electrode active mass loss is higher for UC cells tested at 40°C. Similarly, Q_{SEI} increases with SOC range and C-rate for cells cycling at 40°C, while the increases in Q_{SEI}

are much smaller at 20°C as SOC range increases. The results shown in Figure 15, as well as additional results such as Δ and negative electrode active mass, m_n , can be found in Tables S4 to S9. To better understand the comparison between the lithium inventory loss data from Figures 15b and 15d, the data from Figures 13b and 13d and the data in Figures 5 to 7, Figures S25 to S26 were made. Note that the errors for UC cells are mostly due to capacity versus time extrapolation errors. Additional errors can be caused by uncertainties in the initial positive mass m_{p0} and initial slippage Δ_0 of each cell at $t = 0$ hour, since we only know these values for some of the cells.

For the result in Figure 15, the initial slippage and initial positive mass were fixed to 25 mAh and 1.42 g for all cells as an approximation. Note that the initial slippage of 25 mAh was found to be the smallest initial slippage in Figure S2. If we compare the positive active mass loss and the ΔV related parameter C, we see a linear correlation (see Figure S27). This suggests that positive active mass loss and related electrode damage is a major cause of ΔV growth in these cells. For the interested reader, state of charge maps of our cells can be found in the supplementary material (see Figures S28 and S29).⁵⁶

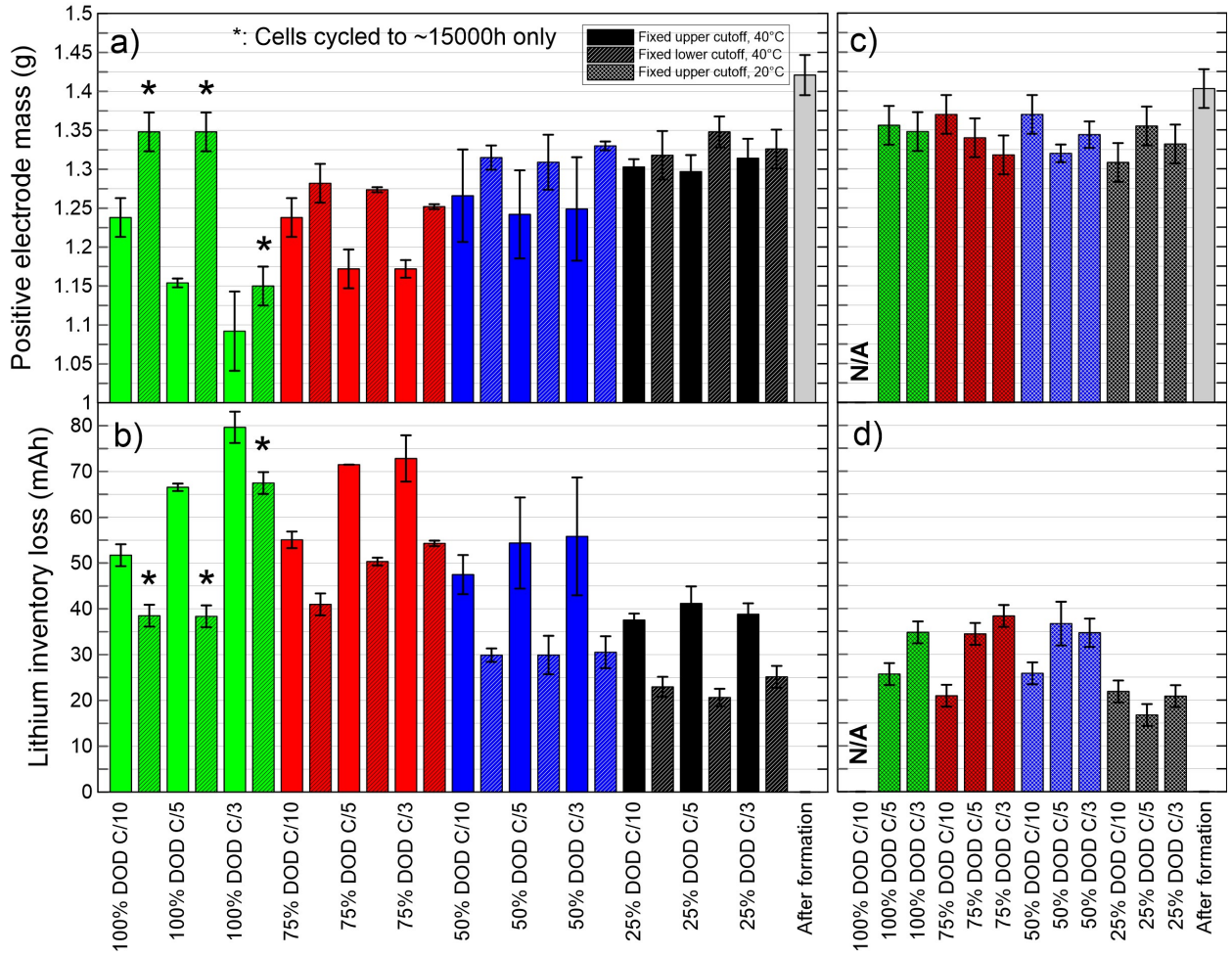


Figure 15: Manual dV/dQ analysis results of UC and LC cells after ~20000h of cycling, except for the indicated cells (*) which cycled only for ~15000h. Subfigures a), c) Positive electrode mass and subfigures b), d) lithium inventory loss is shown. 15a and 15b show results for cells that cycled at 40°C, while subfigures c), d) show results for cells that cycled at 20°C. The initial slippage and the initial positive electrode were both fixed at 25 mAh and 1.42 g for all cells.

Figure 16 shows parameter A ($\text{h}^{-1/2}$) as a function of DOD for cells cycling at C/10 in blue, C/5 in red and C/3 in green obtained by fitting the capacity versus time curves for the checkup cycles of the cells with different models. Equation 1 was used for cells tested at C/10 and 40°C; Equation 3, with no Q_{CV} term was used for cells tested at C/3 and C/5 at 40°C; Equation 7, with

no impedance or Q_{CV} term, was used for cells tested at 20°C at C/10 and Equation 7 with no Q_{CV} term was used for cells tested at 20°C at C/3 or C/5. Figures S5, S31-S32 show the quality of some of these fits. The A parameters of the UC and LC cells are virtually the same at 40°C and increase as the SOC range increases. At 20°C the parameter A is much smaller than at 40°C, as expected, and increases as the SOC range increases. These results indicate that the rate of SEI thickening and inventory loss increases with temperature, C-rate and SOC range. (See Figure S33 for the average voltage vs. time of the UC cells that cycled at 20°C).

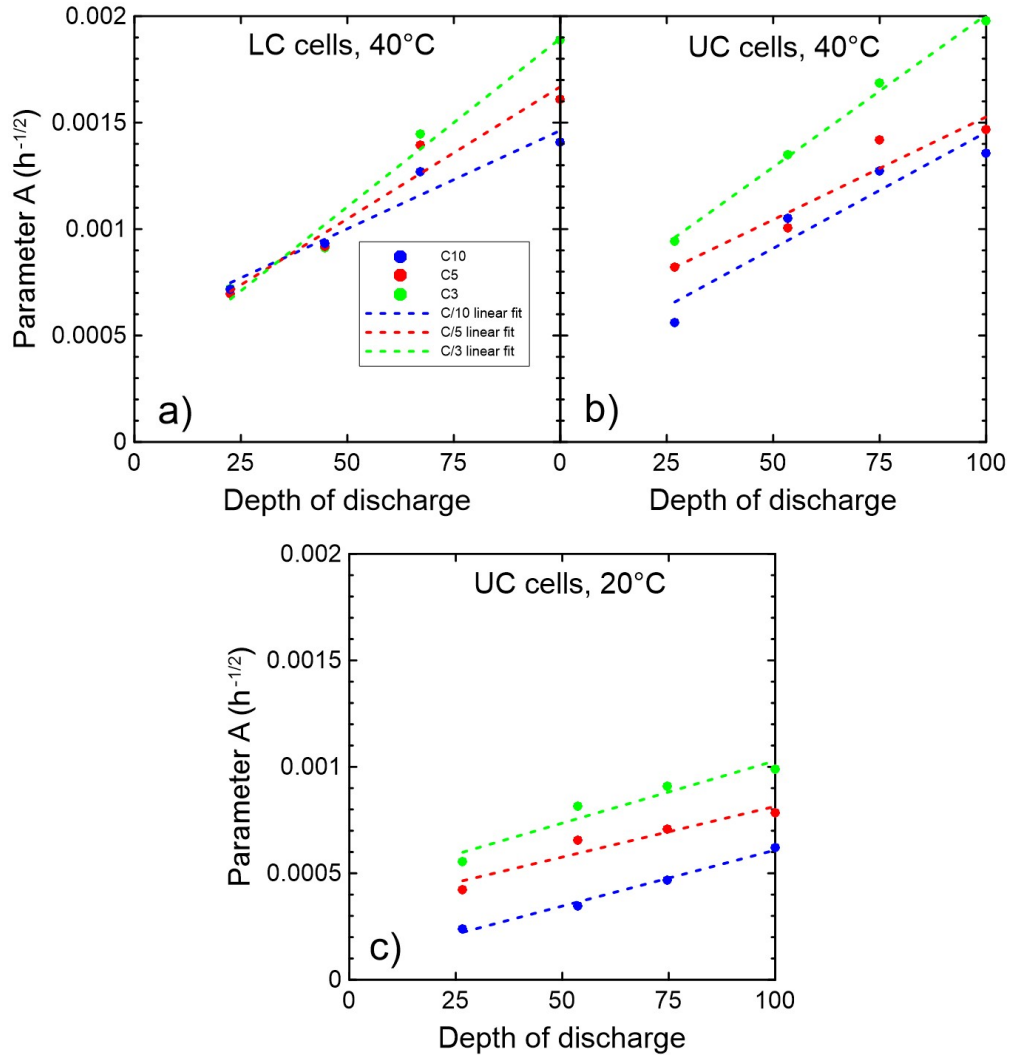


Figure 16: Results of fitting a) LC cells at 40°C, b) UC cells at 40°C and c) UC cells at 20°C using (equation 1), (equation 3) or equation (7) to obtain parameter A. (Equation 1) was used in a) and b) at C/10. The Q_{cv} term was neglected in every case. (Equation 3) was used in subfigures a) and b) at C/5 and C/3, (Equation 7) without the impedance term was used at C/10 in c) and (Equation 7) with the impedance term was used in c) at C/5 and C/3. $\left.\frac{dQ}{dV}\right|_L + \left.\frac{dQ}{dV}\right|_U = 225 \text{ mAh/V}$ was used for all C/5 and C/3 cells. Note that the impedance term was negligible at C/10. C/10 data is in blue, C/5 data is in red and C/3 data is in green.

Figure 17 shows that it is possible to explain and predict the discharge capacity versus time data by fitting the first 2000, 5000 or 6000 hours with a pure lithium inventory loss model (i.e. equation (1)) or by combining the lithium inventory loss term with an impedance term (i.e. equation (3)) and then projecting the fit to the full 20000 hours of data. Since ΔV growth is small at low DOD and C-rate, one can predict the data for the 100% DOD and ~25% DOD cells at C/10 without any impedance term and very little data, as seen in Figures 17a and 17b. Figures 17c and 17d show that adding an impedance term can explain most of the difference between the square root of time model (red dashed lines) and the experimental data (blue lines) for cells tested at C/5 and C/3. Table 3 show the parameters used in those fits. Note that the Q_{CV} term in equation (3) was calculated from the linear fit in Figure S3 for Figures 17c and 17d and was neglected for Figures 17a and 17b. $\left.\frac{dQ}{dV}\right|_L + \left.\frac{dQ}{dV}\right|_U = 225 \text{ mAh/V}$ was used for Figures 17c and 17d. This value can be determined from Figure 1c.

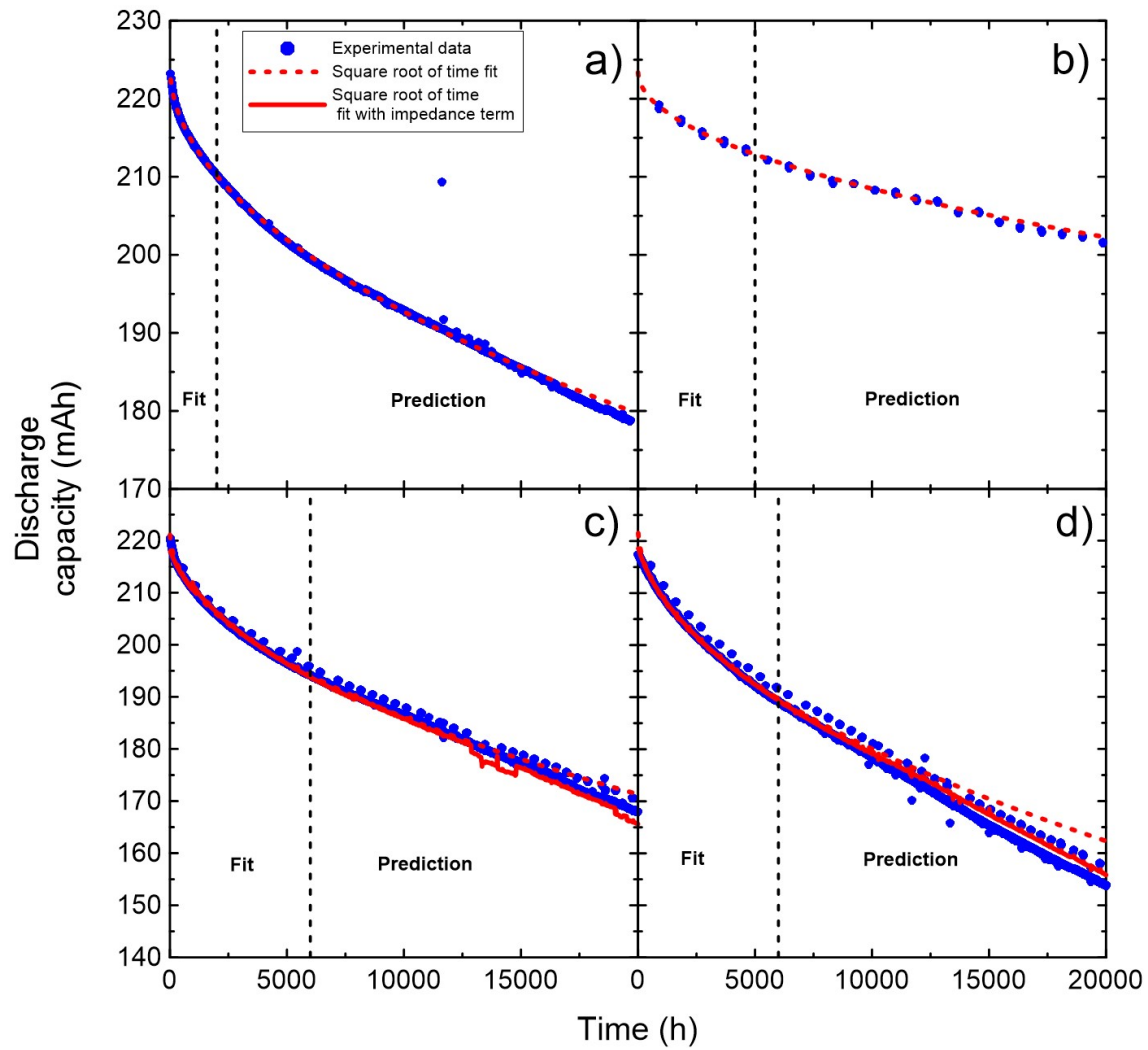


Figure 17: Fitting results for the capacity versus time of LC cells that cycled at 40°C. Cells with the following cycling conditions have been fitted: a) 0-100% SOC C/10, b) 0-25% SOC C/10, c) 0-100% SOC C/5 and d) 0-100% SOC C/3. Results for the square root of time model (red dashed lines) and square root of time models that include an impedance term (red lines) are included and compared to experimental data (blue line). A black vertical dashed line is used to indicate the maximum time used in the fitting of the model to experiment. The model calculation was then projected to times greater than that of the dashed vertical line.

Table 3: Results from the fitting of capacity versus time for UC cells at 40°C in Figure 17 using equations (1) and (3). (NI) means no impedance term was used in the fit (equation 1) and (I) means that an impedance term was used in the fit (equation 3).

Cell protocol and fitting type	Q_0 (mAh)	A ($\text{h}^{-1/2}$)
100% DOD C/10 (NI)	224.2	0.001404
25% DOD C/10 (NI)	223.5	0.0006718
100% DOD C/5 (NI)	221.8	0.001610
100% DOD C/5 (I)	218.6	0.001659
100% DOD C/3 (NI)	222.8	0.001918
100% DOD C/3 (I)	216.3	0.001886

Figure 18 shows the value of the slope of the normalized discharge capacity vs cycle number as a function of DOD at cycle 500 for LC cells that cycled at 40°C, UC cells that cycled at 40°C and UC cells that cycled at 20°C. All the data shown correspond to cells that cycled at C/10. Only the checkup cycles have been included in this analysis. Both the experimental data and the predicted theoretical curve are shown (the equation of the theoretical curve is shown in the Figure, where Q_N is the unitless normalized capacity). The proof for the equation of the theoretical curve can be found in the “Theoretical explanation and proofs” section of the supplementary material. Since the derivative of the normalized capacity with respect to cycle number at time t_1 is quadratic with

DOD (from Figure 16, parameter A is linear with DOD, so A times DOD is quadratic), our research does not contradict the Deshpande-Bernardi model.⁸ In fact, we show in the “Theoretical explanation and proofs” section of the supplementary information that both our model and the Deshpande-Bernardi model are equivalent locally, but that our model is more general (we find that a constant in their models is dependent on time). However, more research is needed to confirm that SEI cracking occurs in our cells.

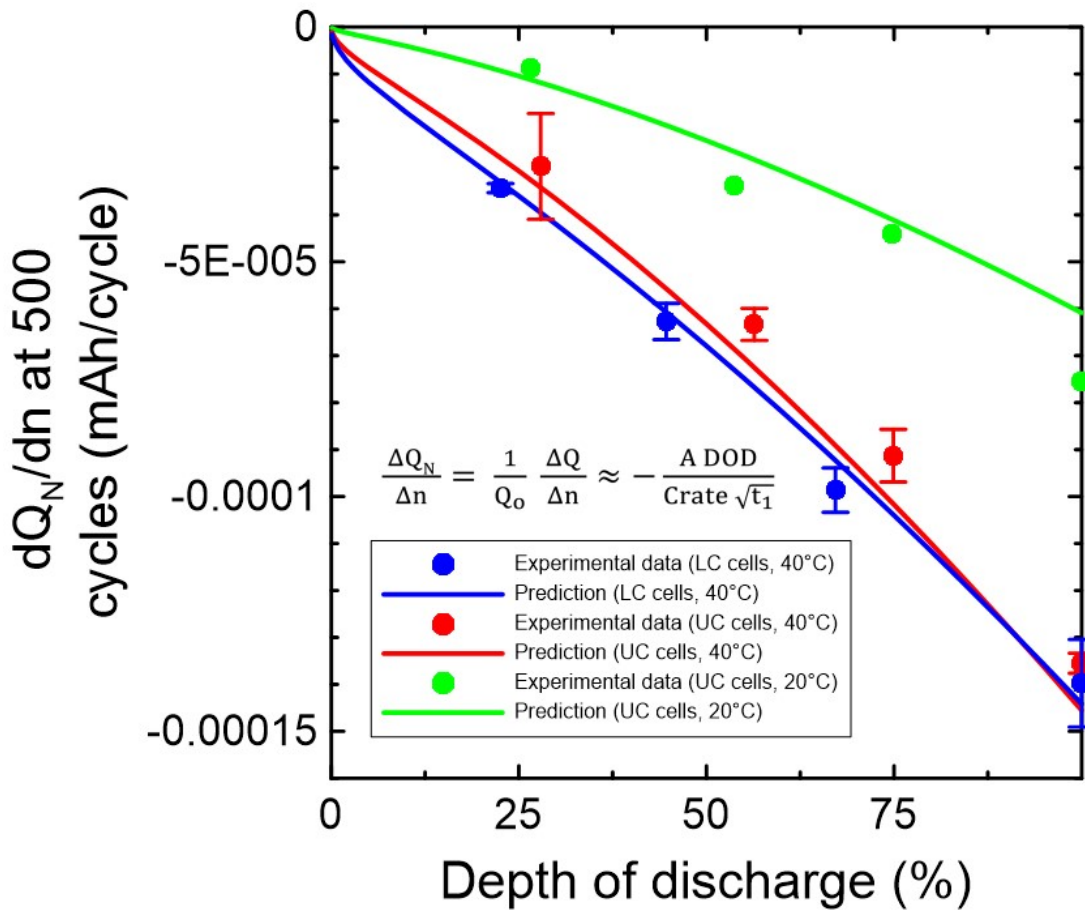


Figure 18: Derivative of normalized capacity with respect to cycle number at cycle number 500 as a function of the depth of discharge. The experimental data of LC at 40°C (in blue), UC cells at 40°C (in red) and UC cells at 20°C (in green) that cycled at C/10 is compared to the theoretical prediction (line of the same colors).

Figure 19a shows that the cell volume change, measured by the Archimedes method, during cycling is closely related to the thickness change, measured with the linear gage, of the jelly roll. In fact, the experimental data closely follow the predicted volume change (black line) which was calculated by multiplying the thickness change by the area of the jelly roll (2.0 cm x 3.0 cm). Most cells showed very little, if any, gas in the gas bags which is consistent with all volume change being due to electrode stack thickness growth. Cells that cycled at 20°C seem to have a larger volume change to thickness change slope which may be due to DMC being used instead of EMC in the electrolyte of the cells tested at 20°C, which may produce more gas during cycling. Figure 19b shows that thickness increase is strongly correlated with the normalized capacity loss during long-term cycling for all types of cells.

Figure 20a shows that the positive electrode active mass loss, from dV/dQ vs. Q analysis, and the thickness increase are approximately quadratically related to each other. This strongly points toward positive electrode thickness increase, which will be confirmed later in this work by X-ray computed tomography (CT). Negative electrode mass loss also seems to be correlated with thickness increase, however the active mass loss at the negative electrode is five times less than at the positive electrode. We will also confirm, using CT scans, that the thickness of the negative electrode increases during cycling, but much less than the positive electrode. Since the cells are balanced to 4.5 V and the maximum voltage of these cells are 4.1 V, the negative electrode has a large excess of graphite and the negative electrode mass loss is too small to affect capacity loss. Since these cells are always anode limited this can only make sense if the negative mass loss occurs in the fully contracted (delithiated) state. Then the lithium coming from the positive electrode during charge will simply find electrically connected graphite particles to intercalate

within. Figures 19 and 20 should convince researchers that measuring cell thickness before and after cycling is important. The raw volume, capacity loss and thickness data can be found in Tables S7 to S9.

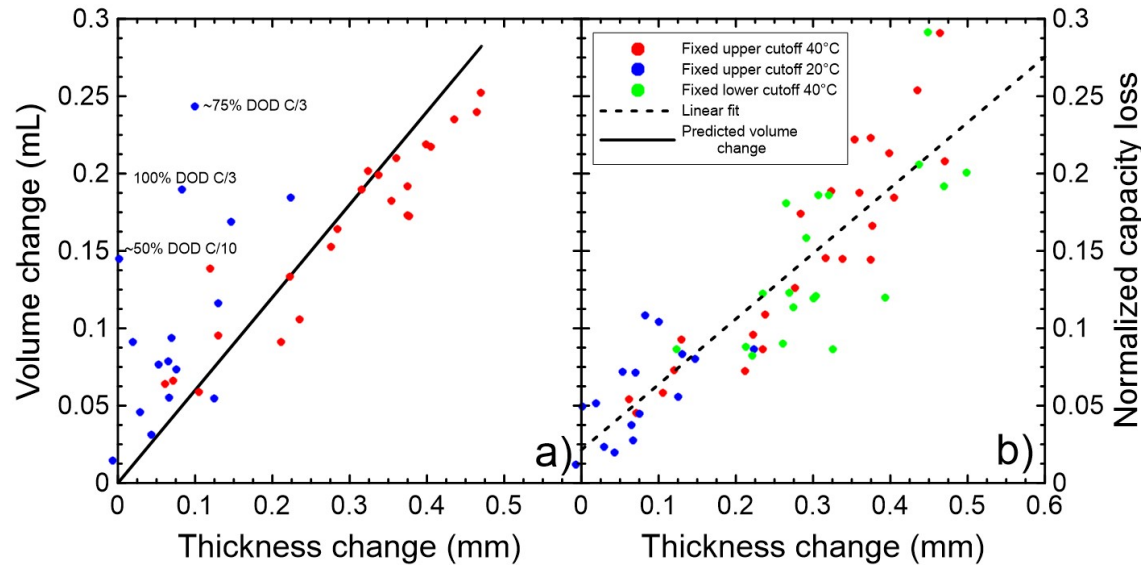


Figure 19: a) Volume change from Archimedes' principle and b) normalized capacity loss after ~20000h of cycling versus thickness change. Red, blue, and green dots indicate UC cells cycling at 40°C, UC cells cycling at 20°C and LC cells cycling at 40°C, respectively.

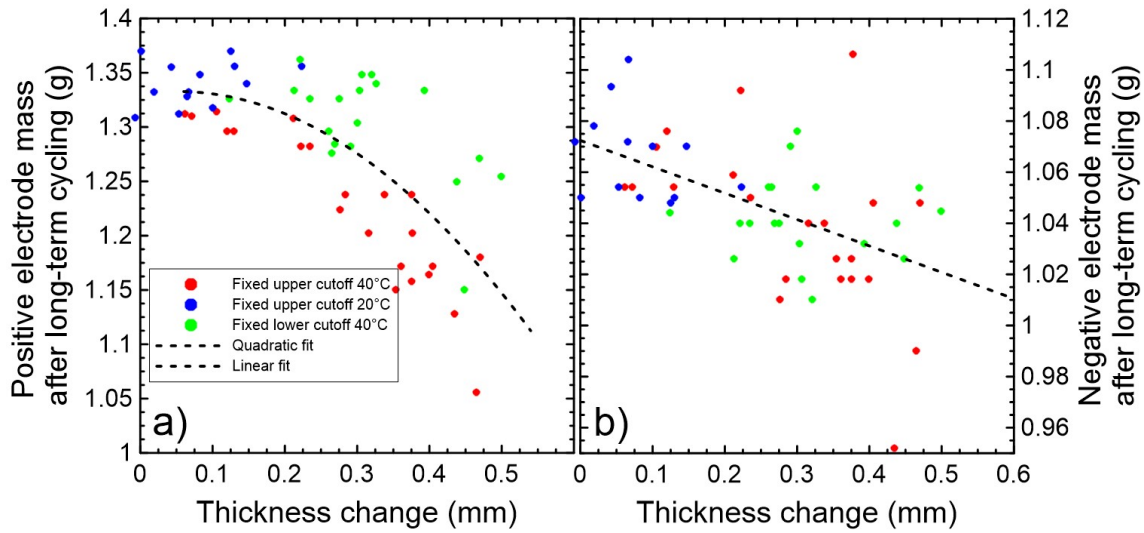


Figure 20: a) Positive and b) negative electrode active mass after ~ 20000 h of cycling versus thickness change of the jelly roll for all UC and LC cells. Red, blue, and green dots indicate UC cells cycling at 40°C , UC cells cycling at 20°C and LC cells cycling at 40°C , respectively. Linear and quadratic fits are also included.

To check if the electrolyte in our cells changed after ~ 20000 hours of cycling, we used Li-ion differential thermal analysis (DTA).³³ Figures 21 to 23 show results from DTA on UC and LC cells. The inverse peak at the highest temperature occurs at the liquidus point of the electrolyte composition-temperature phase diagram.^{33,57,58} The temperature of liquidus feature is very sensitive to the salt concentration and solvent ratios. Since the temperature of the liquidus feature does not vary for cells with the same electrolyte, it can be concluded that changes to the electrolyte are minimal as a function of DOD and C-rate. In addition, the DTA traces in Figures 21 and 22 match quite well to that of a fresh cell after formation, suggesting minimal changes to the electrolyte. There are, however, some slight changes to the DTA signals as the DOD and C-rate both increases. For example, Figures 21 and 22, show that a double peak at approximately -

70°C is present at high C-rate (C/3 and C/5) and high SOC range (0-75%, 25-100% and 0-100%), which is not seen at low C-rate and lower SOC range. This change can be caused by minimal changes in salt and/or solvent concentration. Figures S34 to S36 show an overlap of the DTA spectra of ~25% DOD C/10, 100% DOD C/3 and the fresh cells after formation cells (Figures S34 and S35 only) to better see the differences between them.

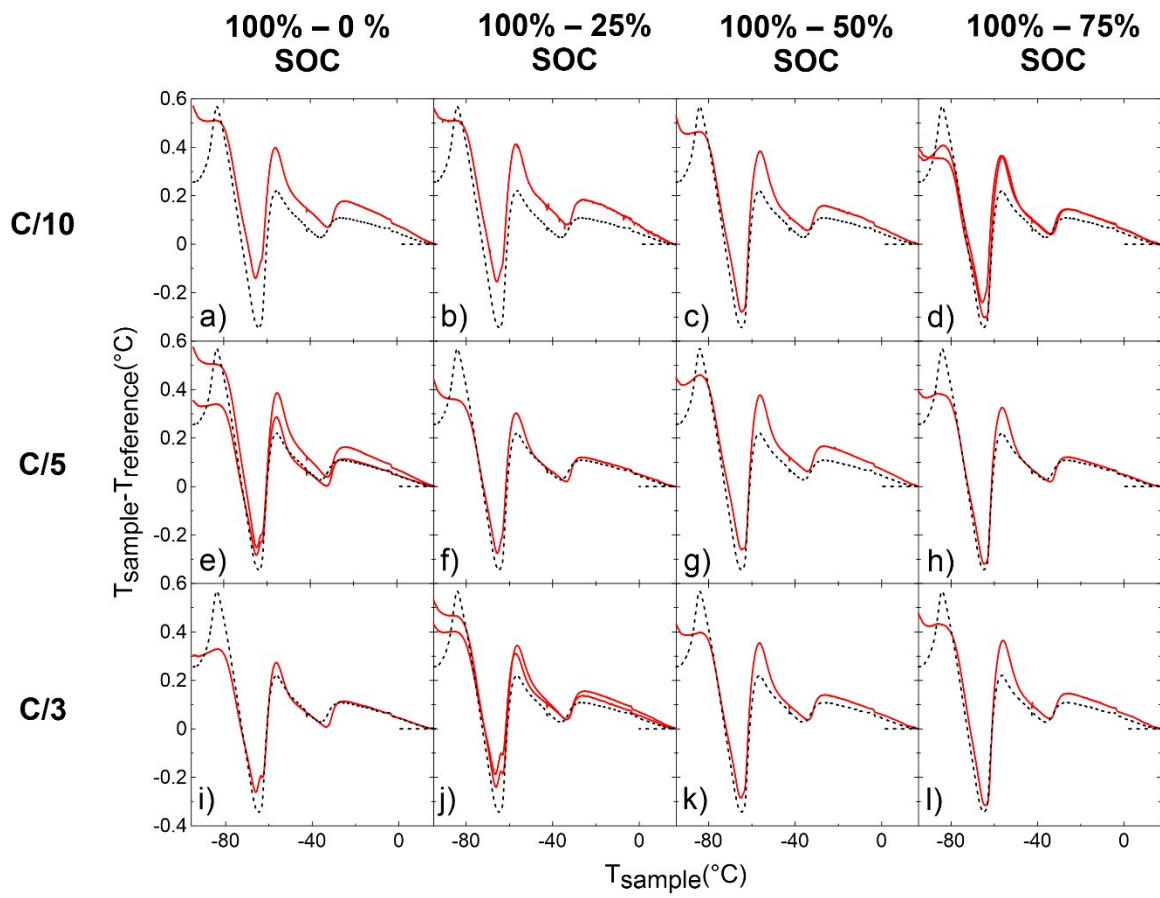


Figure 21: Differential thermal analysis (DTA) versus temperature for UC cells that cycled at 40°C. Columns represent cells that cycled over different SOC ranges, while rows represent cells that cycled at different C-rates. When available the result from a brother cell is shown. The electrolyte originally added to the cells was 1.2M LiPF₆ EC:EMC 3:7 with VC211 (red lines). The red lines show the results after long-term cycling and the black dashed lines show the data of a fresh cell after formation with 1.2M LiPF₆ EC:EMC 3:7 with 2% VC + 1% DTD + 1% MMDS as the electrolyte..

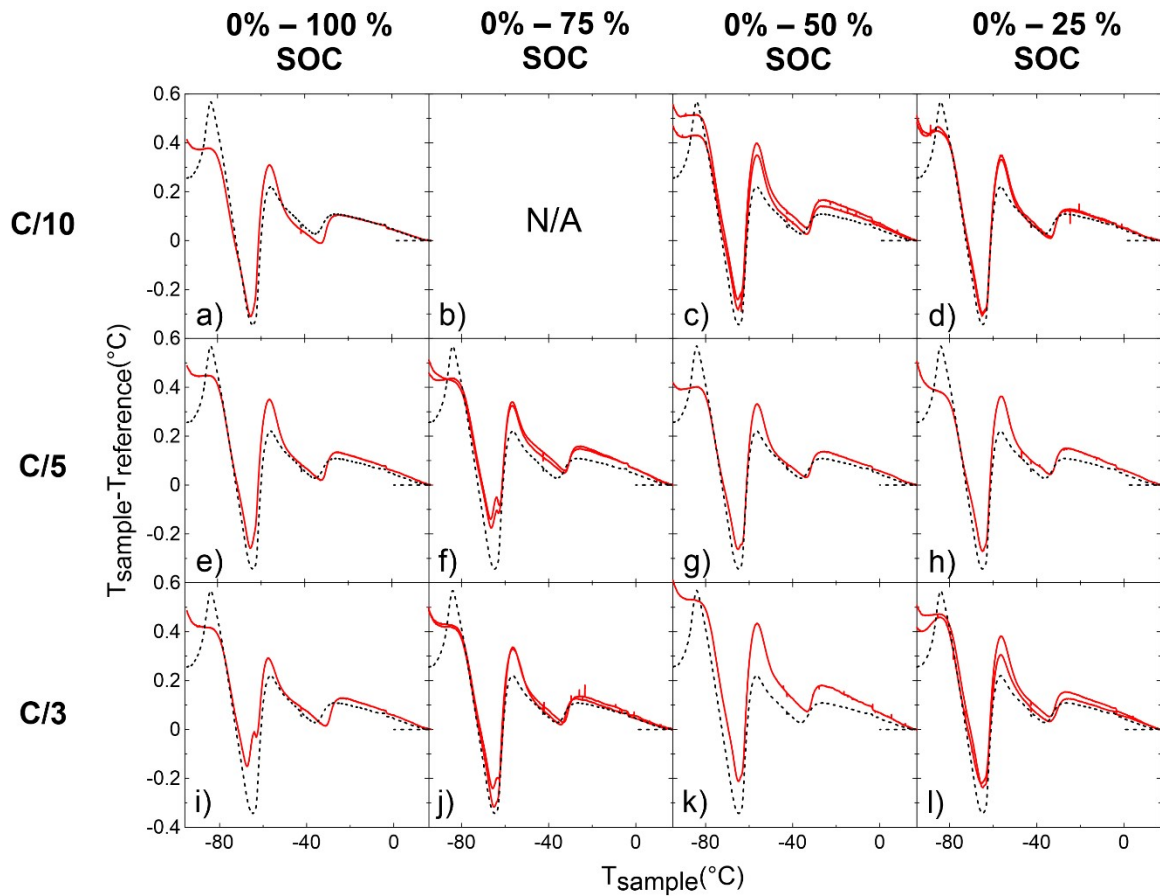


Figure 22: Differential thermal analysis (DTA) versus temperature for LC cells that cycled at 40°C. Columns represent cells that cycled over different SOC ranges, while rows represent cells that cycled at different C-rates. When available the result from a duplicate cell is shown. The electrolyte originally added to the cell was 1.2M LiPF₆ EC:EMC 3:7 with VC211 (red lines). The red lines show the results after long-term cycling and the black dashed lines show the data of a fresh cell after formation with 1.2M LiPF₆ EC:EMC 3:7 with 2% VC + 1% DTD + 1% MMDS as the electrolyte.

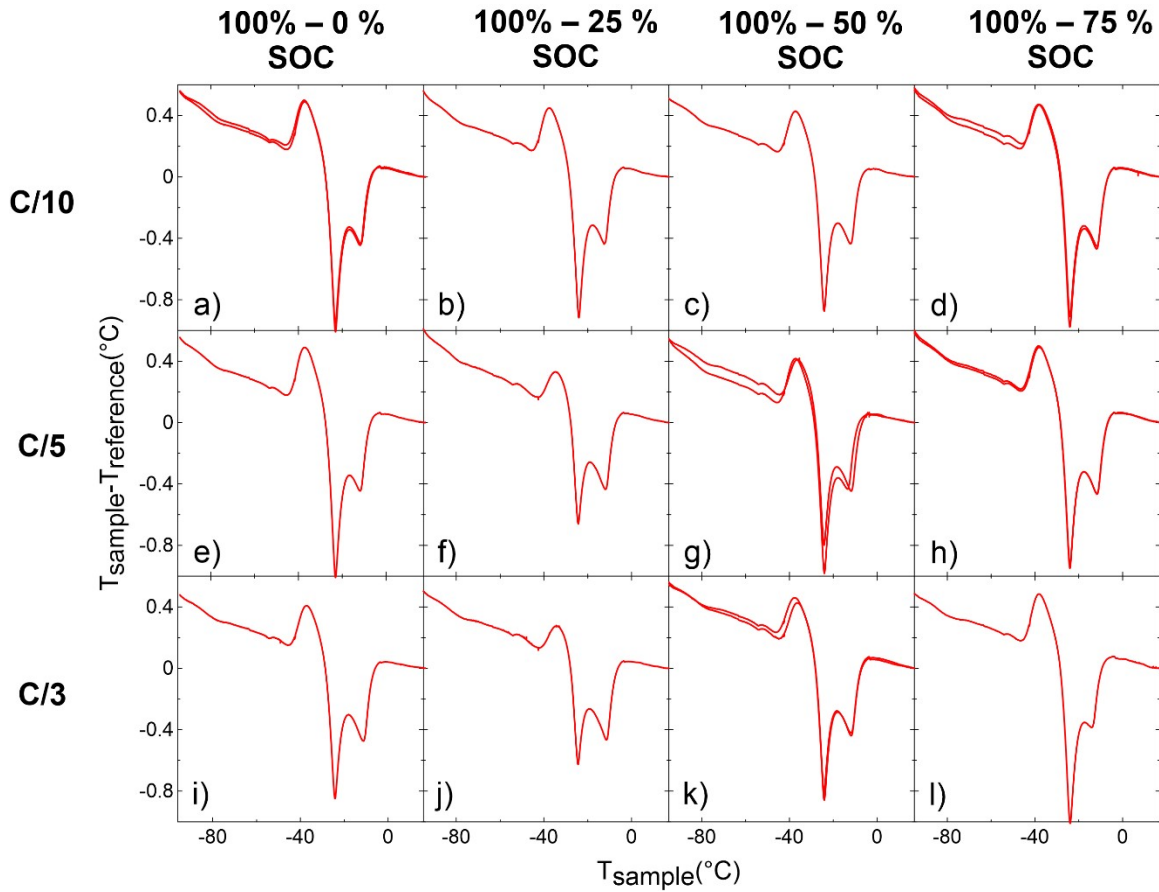


Figure 23: Differential thermal analysis (DTA) versus temperature for UC cells that cycled at 20°C. Columns represent cells that cycled at different SOC ranges while rows represent cells that cycled at different C-rates. When available the results from duplicate cells are shown. The electrolyte originally added to the cell was 1.2M LiPF6 EC:DMC 3:7 with VC211.

Figures 24 to 26 summarize data reported above for the cells tested here and also provide an Ultrasonic image of most of the cells tested. Figures 24 to 26 show that cells with large thickness increase also show the poor transmission to ultrasonic waves. Since volume change and capacity loss correlate with thickness change, they also correlate with poor transmission. We also see that cells with large C-rate and large SOC range during cycling have worse transmission. While it is harder to see any correlation due to missing data in Figure 26, it is thought that transmission is

better at 100% DOD C/3 for cells that cycled at 20°C than at 40°C since the thickness increase is much lower. The curious reader can have a look at the impact of cell voltage on ultrasonic transmission in Figures S37 and S38.

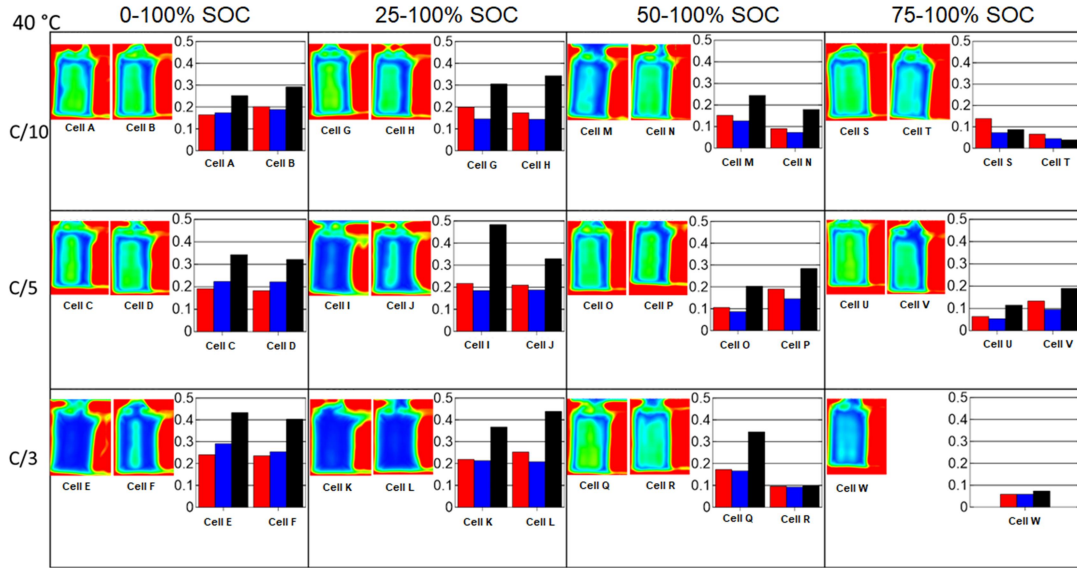


Figure 24: Ultrasonic transmission results for UC cells that cycled at 40°C for 20000 h. Columns represent cells that cycled over different SOC ranges, while rows represent cells that cycled at different C-rates. The bar graphs show, in order, the true volume change in mL from Archimedes principle (red), the normalized capacity loss (blue) and the change in thickness in mm (black). When available the results from duplicate cells are shown. In the Ultrasonic color maps, red represents no attenuation, green represents high transmission and blue represents low transmission.

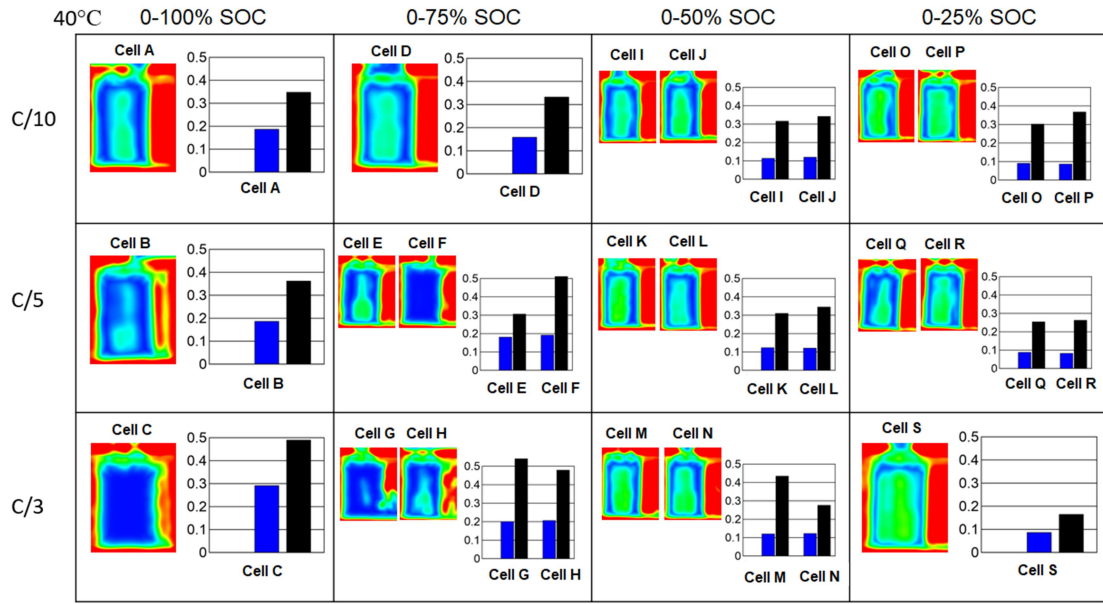


Figure 25: Ultrasonic transmission results for multiple LC cells that cycled at 40°C for 20000 h.

Columns represent cells that cycled at different SOC ranges, while rows represent cells that cycled at different C-rates. The bar graphs show, in order, the normalized capacity loss (blue) and the change in thickness in mm (black). When available the results from duplicate cells are shown. In the Ultrasonic color maps, red represents no attenuation, green represents high transmission and blue represents low transmission.

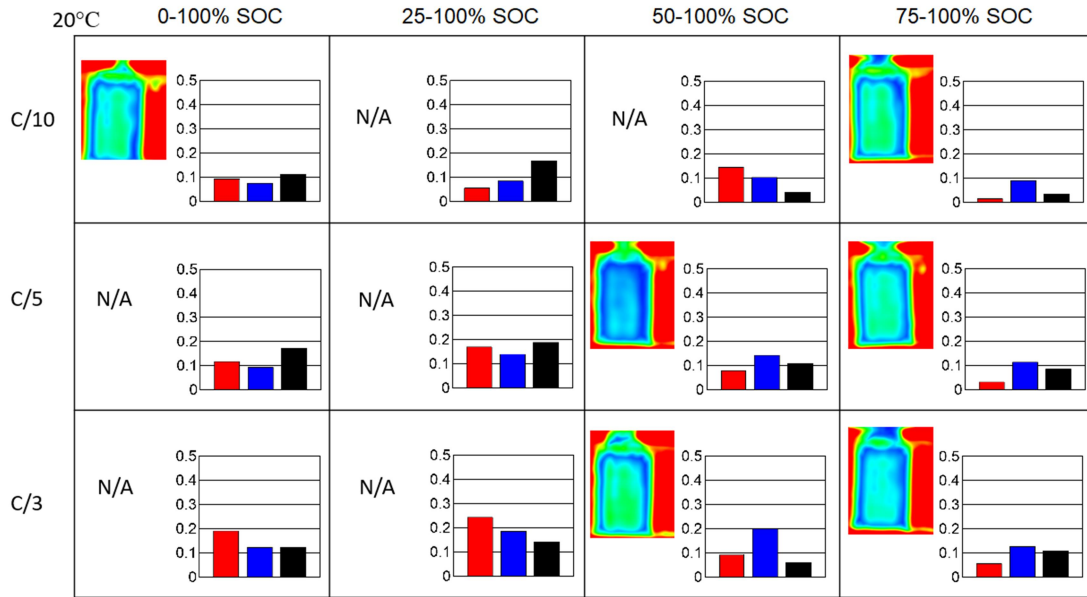


Figure 26: Ultrasonic transmission results for multiple UC cells that cycled at 20°C for 20000 h.

Columns represent cells that cycled at different SOC ranges, while rows represent cells that cycled at different C-rates. The bar graphs show, in order, the true volume change in mL from Archimedes principle (red), the normalized capacity loss (blue) and the change in thickness in mm (black). In the Ultrasonic color maps, red represents no attenuation, green represents high transmission and blue represents low transmission.

The results in Figures 24-26 can be understood based on the work by Deng et al.³⁴ Cells that have a large thickness increase do not have enough electrolyte to fill the increased pore volume. This “unwetting” leads to poor ultrasonic transmission. A careful examination of Figures 24-26 shows that cells which generally had a large thickness increase (length of black bar in the Figures) had poor ultrasonic transmission (Blue color).

Figure 27 shows X-ray computed tomography scans of a fresh cell and a cell after 20000 h of testing. The thickness of the double-side coated positive electrode was measured at three

positions in the cell and the thickness of the separator plus double-side coated negative electrode was also measured at several locations. The 75% DOD UC cell that cycled at C/3 had a 39% increase in its positive electrode thickness and a 10% increase in its negative electrode thickness when compared to a control cell that was only charged once (i.e. formation). This agrees with Figure 20. Visible deformation of the jelly roll is also visible for the cycled cell vs the control, where the relatively smooth curvature about the turn becomes rigid and angular after cycling (especially for the innermost layer). The increase in electrode thickness with cycling also appears to have filled in the “empty” region at the center of the jelly roll. X-ray CT scans on more cells from this study will be carried out in future work.

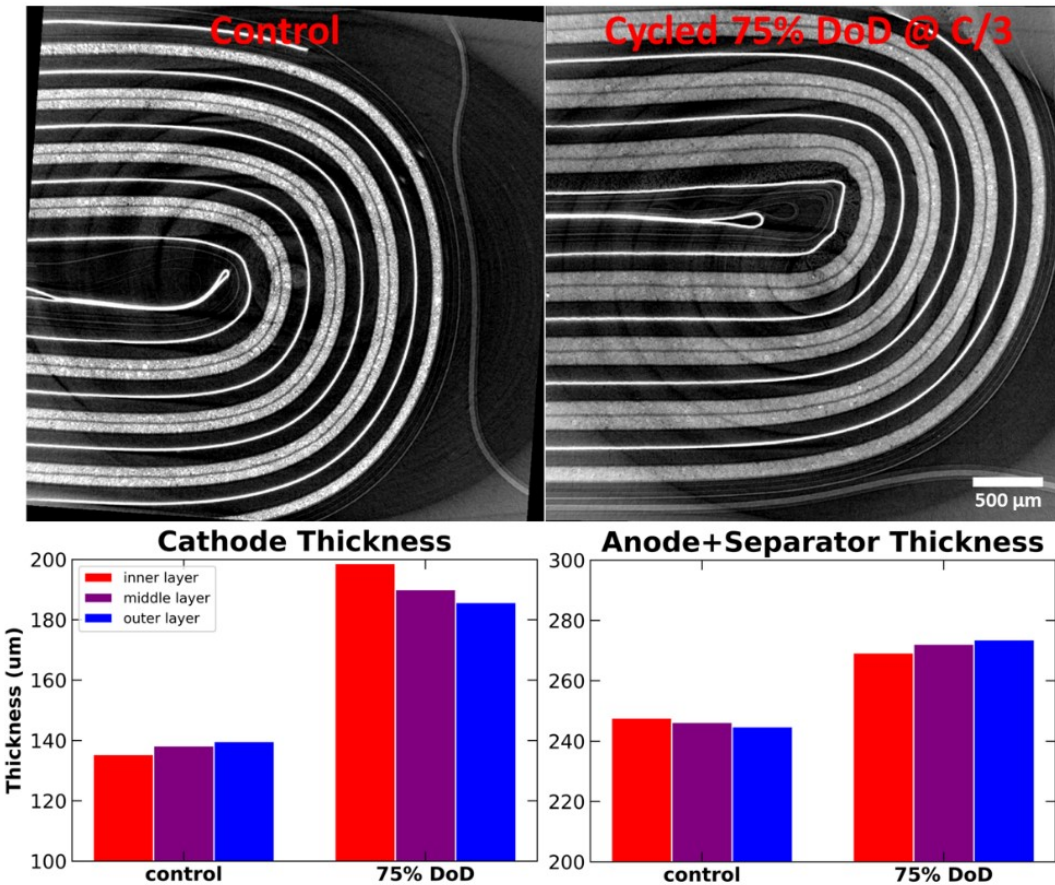


Figure 27: The upper left side of the Figure shows a CT-scan of a NMC622/NG that only went through formation (control cell), while the upper right side of the Figure shows a CT-scan of a UC cell that cycled at between 25 and 100% SOC at C/3 and 40°C for 20000h. The CT scans are presented as absorption images, where the graphite anode and separator are dark (low x-ray absorption) while the copper current collector between the two graphite layers shows as a bright line (high x-ray absorption). The positive electrode layers are relatively bright and the aluminum foil between them is less bright. The lower part of the Figure shows the cathode thickness and anode + separator thickness of the same control and 75% DOD cells. Most of the thickness increase comes from the cathode (39% increase vs 10% for the anode)

The cell cycled at 40°C with a 25-100% SOC range described in Figure 27 also had a large positive electrode active mass loss of 16 percent as shown in Table S4 (assuming an initial positive active mass of 1.4 g). It is likely that the positive electrode active mass loss and positive electrode thickness expansion are related. Microcracking of the electrode particles will cause thickness increase and active mass loss.

Figure 28 shows X-ray CT scans focused at the edge of the jelly roll to examine the amount of electrolyte that can be observed outside the jelly roll. Figure 28 shows that after cells cycle for 20000 h at 40°C over a large SOC range that no electrolyte is visible outside the jelly roll. By contrast, some electrolyte can be observed outside the jelly roll for cells cycled over a 25% SOC range where cell thickness expansion is less. This explains why the transmission of ultrasonic waves is poor for cells that cycled the most times (C/3 and C/5) over large SOC ranges at 40°C, since there may not be enough electrolyte available to fill the expanded pore spaces even though all available electrolyte has been “sucked” into the jelly roll.³⁴ The increase in electrode thicknesses causes the pore volume inside the electrodes to increase. The electrolyte then fills as much of the empty space inside the electrodes as possible like a sponge, explaining why no electrolyte is observed outside the jelly roll for the cells cycled over large SOC range.

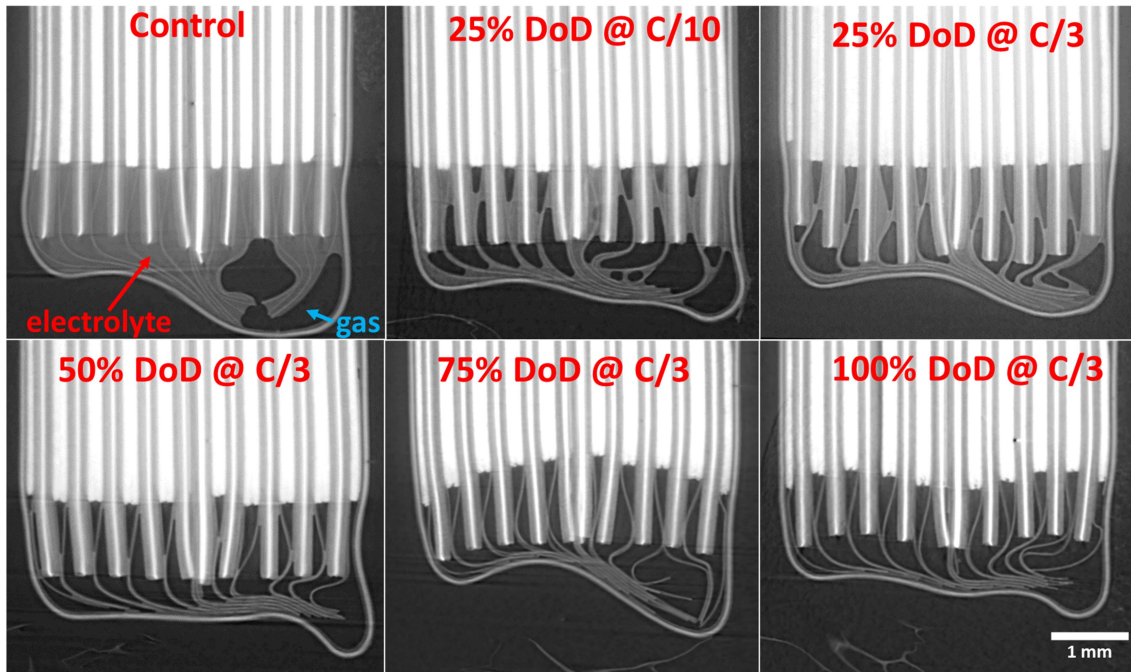


Figure 28: CT-scans of a control cell (immediately after formation), UC cells that cycled at 100-75% SOC C/10, at 100-75% SOC C/3, at 100-50% SOC C/3, at 100-25% SOC C/3 and 100-0% SOC C/3. The electrolyte appears as light gray regions outside the jelly roll and gas or vacuum appear as black regions. The white regions represent the electrode of the cells. The plastic casing of the cells and the separators extending beyond the electrodes are also seen as light grey.

Discussion

Assuming an electric vehicle with a 400 km range and a battery using the NMC622/NG VC211 chemistry described here, a 25% SOC cycle will allow a 100 km range. At 20°C, after ~12200 cycles, a 25% DOD charge at C/3 still allow ~96 km (4% loss) according to Figure 29a. If one 25% SOC range C/3 cycle occurs each day, 12200 cycles correspond to 33 years and a minimum of 1.20 million of kilometers to 96% capacity. Note that Figure 7 shows virtually no impedance growth for this cell, Figure 23 shows no change to the electrolyte and Figure 26 and Table S9 show virtually no thickness change to this cell. This suggests the cell could continue in this mode

for many more cycles. If one did a 100% DOD charge every two months (like our experiment), this will result in a ~380 km full range after the same amount of time according to Figure 29b. One could imagine that cycling Harlow et al. cells over a 25% SOC range would result in an even better long-term performance than shown in Figure 29.²⁷

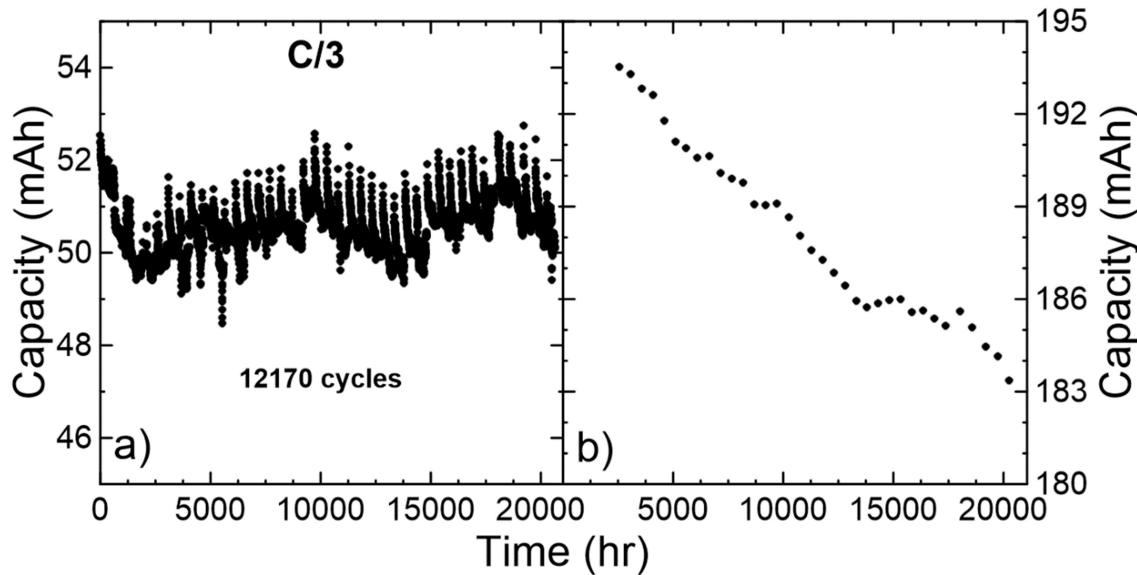


Figure 29: Discharge capacity versus time for a 100-75% SOC C/3 UC cell that cycled at 20°C. Subfigure a) shows the 100-75% SOC C/3 cycles of that cell, while subfigure b) shows the 100% DOD C/10 checkup cycles of that cell.

Conclusions

The above work can be summarized by the following conclusions:

- Capacity loss in these polycrystalline NMC622/NG pouch cells results primarily from lithium inventory loss due to negative electrode SEI growth. Even though there is positive electrode active mass loss, these cells remain anode limited so the positive active mass loss does not **directly** contribute to capacity fade.

- Capacity versus time predictions can be improved by adding an impedance term to a simple $t^{1/2}$ lithium inventory loss model.
- Lithium inventory loss increases when the SOC range increases.
- Lithium inventory loss is worse at high temperature. However, UC cells and LC cells with the same SOC range have similar lithium inventory loss.
- Impedance growth and impedance related capacity loss are worse at higher temperature and higher DOD.
- Positive active mass loss is worse at high temperature and worse at higher DOD.
- Capacity loss and jelly roll thickness increase are correlated.
- Positive active mass loss, jelly roll thickness increase and impedance growth are correlated.
- X-ray CT-scans show that most of the jelly roll thickness increase comes from the positive electrode.
- Our work doesn't contradict the SEI cracking model of Deshpande and Bernardi.⁸
- The increase in electrode thicknesses causes the pore volume inside the electrodes to increase. The electrolyte then fills as much of the empty space inside the electrodes as possible like a sponge, explaining why no electrolyte is observed outside the jelly roll for the cells cycled over a large SOC range. If stack expansion continues further, this will eventually cause, presumably dramatic, cell failure by “unwetting”.
- Poor ultrasonic transmission at large SOC range and C-rate can be explained by the lower amount of electrolyte available to fill the expanded electrode pore spaces.
- Since the temperature of the liquidus feature does not vary for cells with the same electrolyte and the DTA traces of most cells match the DTA traces of fresh cells after

formation, it can be concluded that changes to the electrolyte are minimal as a function of DOD and C-rate under the conditions probed here.

In our opinion, the NMC622/NG cells presented here do not represent the state of the art in terms of capacity retention versus cycle number or time. They are less impressive than the single crystal NMC532/AG (artificial graphite) cells described by Harlow et al.²⁷ and by Cheng et al.⁵⁹ There are two main reasons for this. First, the polycrystalline NMC622 positive electrode swells substantially during extended cycling and this is worse as the SOC range is increased. By contrast, as we will show in an upcoming publication, the single crystal NMC532 electrode shows virtually no swelling after the same number of cycles under the same conditions. Second, the natural graphite electrode material used in the NMC622/NG cells has been shown to be inferior to the artificial graphite used in the single crystal NMC532/AG cells in terms of swelling and rate of Li inventory loss.²⁶ It is quite interesting that even with the relatively worse performance of the polycrystalline NMC622/NG cells, our estimates show that this chemistry would still be fully suitable for electric vehicles that spent much of the time doing low DOD drives. This is one reason that virtually any Li-ion cell of relatively decent quality is sufficient for typical EV use.

Acknowledgement

The authors acknowledge the financial support of NSERC and Tesla Canada under the auspices of the Industrial Research Chair program. A. Louli acknowledges scholarship support from NSERC.

References

1. D. S. Hall, T. Hynes, and J. R. Dahn, *J. Electrochem. Soc.*, **165**, A2961–A2967 (2018).
2. J. Xia, L. Ma, and J. R. Dahn, *J. Power Sources*, **287**, 377–385 (2015).
3. F. Bian, Z. Zhang, and Y. Yang, *J. Energy Chem.*, **23**, 383–390 (2014).
4. K. Wang, L. Xing, Y. Zhu, X. Zheng, D. Cai, and W. Li, *J. Power Sources*, **342**, 677–684 (2017).
5. J. Smart, W. Powell, and S. Schey, in, p. 2013-01–1441 (2013) <https://www.sae.org/content/2013-01-1441/>.
6. P. Plötz, N. Jakobsson, and F. Sprei, *Transp. Res. Part B Methodol.*, **101**, 213–227 (2017).
7. N. S. Pearre, W. Kempton, R. L. Guensler, and V. V. Elango, *Transp. Res. Part C Emerg. Technol.*, **19**, 1171–1184 (2011).
8. R. D. Deshpande and D. M. Bernardi, *J. Electrochem. Soc.*, **164**, A461–A474 (2017).
9. Y. Preger, H. M. Barkholtz, A. Fresquez, D. L. Campbell, B. W. Juba, J. Romàn-Kustas, S. R. Ferreira, and B. Chalamala, *J. Electrochem. Soc.*, **167**, 120532 (2020).
10. L. Willenberg, P. Dechent, M. Eckert, D. Sauer, and E. Figgemeier, *Systematic Investigation of Mechanical Ageing of High Energy Lithium-Ion Batteries*, (2019).
11. X. M. Liu and C. B. Arnold, *J. Electrochem. Soc.*, **163**, A2501 (2016).
12. A. Maheshwari, M. Heck, and M. Santarelli, *Electrochimica Acta*, **273**, 335–348 (2018).
13. J. Wang, P. Liu, J. Hicks-Garner, E. Sherman, S. Soukiazian, M. Verbrugge, H. Tataria, J. Musser, and P. Finamore, *J. Power Sources*, **196**, 3942–3948 (2011).
14. E. Sarasketa-Zabala, I. Gandiaga, E. Martinez-Laserna, L. M. Rodriguez-Martinez, and I. Villarreal, *J. Power Sources*, **275**, 573–587 (2015).
15. S. Watanabe, M. Kinoshita, T. Hosokawa, K. Morigaki, and K. Nakura, *J. Power Sources*, **260**, 50–56 (2014).
16. J. Li, J. Harlow, N. Stakheiko, N. Zhang, J. Paulsen, and J. Dahn, *J. Electrochem. Soc.*, **165**, A2682 (2018).
17. Y. Zhang, R. Xiong, H. He, X. Qu, and M. Pecht, *Appl. Energy*, **255**, 113818 (2019).
18. J. de Hoog, J.-M. Timmermans, D. Ioan-Stroe, M. Swierczynski, J. Jaguemont, S. Goutam, N. Omar, J. Van Mierlo, and P. Van Den Bossche, *Appl. Energy*, **200**, 47–61 (2017).
19. Y. Gao, J. Jiang, C. Zhang, W. Zhang, and Y. Jiang, *J. Power Sources*, **400**, 641–651 (2018).

20. M. Lewerenz, J. Münnix, J. Schmalstieg, S. Käbitz, M. Knips, and D. U. Sauer, *J. Power Sources*, **345**, 254–263 (2017).
21. Y. Cui, C. Du, G. Yin, Y. Gao, L. Zhang, T. Guan, L. Yang, and F. Wang, *J. Power Sources*, **279**, 123–132 (2015).
22. K. Darcovich, S. Recoskie, and F. Fattal, *J. Appl. Electrochem.*, **50**, 111–124 (2020).
23. F. Single, A. Latz, and B. Horstmann, *ChemSusChem*, **11**, 1950–1955 (2018).
24. K. Ushirogata, K. Sodeyama, Z. Futera, Y. Tateyama, and Y. Okuno, *J. Electrochem. Soc.*, **162**, A2670 (2015).
25. D. Y. Wang, J. Xia, L. Ma, K. J. Nelson, J. E. Harlow, D. Xiong, L. E. Downie, R. Petibon, J. C. Burns, A. Xiao, W. M. Lamanna, and J. R. Dahn, *J. Electrochem. Soc.*, **161**, A1818–A1827 (2014).
26. S. L. Glazier, J. Li, A. J. Louli, J. P. Allen, and J. R. Dahn, *J. Electrochem. Soc.*, **164**, A3545 (2017).
27. J. E. Harlow, X. Ma, J. Li, E. Logan, Y. Liu, N. Zhang, L. Ma, S. L. Glazier, M. M. E. Cormier, M. Genovese, S. Buteau, A. Cameron, J. E. Stark, and J. R. Dahn, *J. Electrochem. Soc.*, **166**, A3031–A3044 (2019).
28. L. Ma, S. Young, L. D. Ellis, Q. Huang, X. Ma, M. Chatzidakis, H. Li, L. Thompson, A. Eldesoky, C. R. M. McFarlane, G. A. Botton, I. G. Hill, and J. R. Dahn, *ACS Appl. Energy Mater.*, **1**, 7052–7064 (2018).
29. S.-T. Myung, K. Izumi, S. Komaba, Y.-K. Sun, H. Yashiro, and N. Kumagai, *Chem. Mater.*, **17**, 3695–3704 (2005).
30. T. M. Bond, J. C. Burns, D. A. Stevens, H. M. Dahn, and J. R. Dahn, *J. Electrochem. Soc.*, **160**, A521–A527 (2013).
31. H. M. Dahn, A. J. Smith, J. C. Burns, D. A. Stevens, and J. R. Dahn, *J. Electrochem. Soc.*, **159**, A1405–A1409 (2012).
32. MATLAB, 9.8.0.1417392 (R2020a), The MathWorks Inc., Natick, Massachusetts, (2020).
33. R. P. Day, J. Xia, R. Petibon, J. Rucska, H. Wang, A. T. B. Wright, and J. R. Dahn, *J. Electrochem. Soc.*, **162**, A2577 (2015).
34. Z. Deng, Z. Huang, Y. Shen, Y. Huang, H. Ding, A. Luscombe, M. Johnson, J. E. Harlow, R. Gauthier, and J. R. Dahn, *Joule*, **4**, 2017–2029 (2020).
35. T. W. Wysokinski, D. Chapman, G. Adams, M. Renier, P. Suortti, and W. Thomlinson, *Nucl. Instrum. Methods Phys. Res. Sect. Accel. Spectrometers Detect. Assoc. Equip.*, **775**, 1–4 (2015).
36. M. Vogelgesang, T. Farago, T. F. Morgeneyer, L. Helfen, T. dos Santos Rolo, A. Myagotin, and T. Baumbach, *J. Synchrotron Radiat.*, **23**, 1254–1263 (2016).
37. A. J. Louli, J. Li, S. Trussler, C. R. Fell, and J. R. Dahn, *J. Electrochem. Soc.*, **164**, A2689–A2696 (2017).

38. M. Petit, E. Prada, and V. Sauvant-Moynot, *Appl. Energy*, **172**, 398–407 (2016).
39. M. Schimpe, M. E. von Kuepach, M. Naumann, H. C. Hesse, K. Smith, and A. Jossen, *J. Electrochem. Soc.*, **165**, A181 (2018).
40. K. Smith, A. Saxon, M. Keyser, B. Lundstrom, Ziwei Cao, and A. Roc, in *2017 American Control Conference (ACC)*, p. 4062–4068 (2017).
41. A. Jokar, B. Rajabloo, M. Désilets, and M. Lacroix, *J. Power Sources*, **327**, 44–55 (2016).
42. Y. Li, K. Liu, A. M. Foley, A. Zülke, M. Berecibar, E. Nanini-Maury, J. Van Mierlo, and H. E. Hoster, *Renew. Sustain. Energy Rev.*, **113**, 109254 (2019).
43. K. A. Severson, P. M. Attia, N. Jin, N. Perkins, B. Jiang, Z. Yang, M. H. Chen, M. Aykol, P. K. Herring, D. Fragedakis, M. Z. Bazant, S. J. Harris, W. C. Chueh, and R. D. Braatz, *Nat. Energy*, **4**, 383–391 (2019).
44. A. J. Smith, J. C. Burns, X. Zhao, D. Xiong, and J. R. Dahn, *J. Electrochem. Soc.*, **158**, A447–A452 (2011).
45. R. Fathi, J. C. Burns, D. A. Stevens, H. Ye, C. Hu, G. Jain, E. Scott, C. Schmidt, and J. R. Dahn, *J. Electrochem. Soc.*, **161**, A1572 (2014).
46. P. M. Attia, W. C. Chueh, and S. J. Harris, *J. Electrochem. Soc.*, **167**, 090535 (2020).
47. X. Ma, J. E. Harlow, J. Li, L. Ma, D. S. Hall, S. Buteau, M. Genovese, M. Cormier, and J. R. Dahn, *J. Electrochem. Soc.*, **166**, A711–A724 (2019).
48. B. Gyenes, D. A. Stevens, V. L. Chevrier, and J. R. Dahn, *J. Electrochem. Soc.*, **162**, A278 (2014).
49. W. Lee, S. Muhammad, T. Kim, H. Kim, E. Lee, M. Jeong, S. Son, J.-H. Ryou, and W.-S. Yoon, *Adv. Energy Mater.*, **8**, 1701788 (2018).
50. L. Willenberg, P. Dechent, G. Fuchs, M. Teuber, M. Eckert, M. Graff, N. Kürten, D. U. Sauer, and E. Figgemeier, *J. Electrochem. Soc.*, **167**, 120502 (2020).
51. P. Yan, J. Zheng, M. Gu, J. Xiao, J.-G. Zhang, and C.-M. Wang, *Nat. Commun.*, **8** (2017) <https://www.ncbi.nlm.nih.gov/pmc/articles/PMC5241805/>.
52. M. Ecker, N. Nieto, S. Käbitz, J. Schmalstieg, H. Blanke, A. Warnecke, and D. U. Sauer, *J. Power Sources*, **248**, 839–851 (2014).
53. R. D. Deshpande and K. Uddin, *J. Energy Storage*, **33**, 101932 (2021).
54. J. Marcos, I. De la Parra, M. García, and L. Marroyo, *Energies*, **7**, 6593–6619 (2014).
55. G. Gruber, V. Calderaro, V. Galdi, and A. Piccolo, *Electronics*, **9**, 939 (2020).
56. J. Christensen and J. Newman, *J. Electrochem. Soc.*, **152**, A818 (2005).
57. M. S. Ding, K. Xu, and T. R. Jow, *J. Electrochem. Soc.*, **147**, 1688 (2000).

58. M. S. Ding, K. Xu, S. Zhang, and T. R. Jow, *J. Electrochem. Soc.*, **148**, A299 (2001).
59. J. H. Cheng, J. E. Harlow, M. B. Johnson, R. Gauthier, and J. R. Dahn, *J. Electrochem. Soc.*, **167**, 130529 (2020).